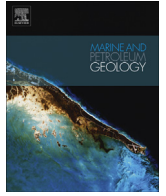




ELSEVIER

Contents lists available at ScienceDirect

Marine and Petroleum Geology

journal homepage: www.elsevier.com/locate/marpetgeo

Research paper

Provenance identification and sedimentary analysis of the beach and bar systems in the Palaeogene of the Enping Sag, Pearl River Mouth Basin, South China Sea



Qianghu Liu ^{a, b, *}, Hongtao Zhu ^{c, d, **}, Yu Shu ^e, Xiaomin Zhu ^{a, b}, Xianghua Yang ^{c, d},
Liang Chen ^f, Mingxuan Tan ^{a, b}, Mingyang Geng ^f

^a Faculty of Geoscience, State Key Laboratory of Petroleum Resources and Processing, China University of Petroleum, Beijing 102249, China

^b College of Geosciences, China University of Petroleum, Beijing 102249, China

^c Key Laboratory of Tectonics and Petroleum Resources, China University of Geosciences, Ministry of Education, Wuhan 430074, Hubei, China

^d Faculty of Earth Resources, China University of Geosciences, Wuhan 430074, China

^e China National Offshore Oil Corporation Limited-Shenzhen, Guangzhou 510240, China

^f China National Offshore Oil Corporation Research Institute, Beijing 100027, China

ARTICLE INFO

Article history:

Received 10 July 2015

Received in revised form

28 November 2015

Accepted 1 December 2015

Available online 9 December 2015

Keywords:

Provenance

Beach and bar systems

Detrital zircon

Seismic multi-attribute

Palaeogene

Enping sag

ABSTRACT

During deposition in the Palaeogene, the Pearl River Mouth Basin (Enping Sag) was filled by sediments derived from northern and southern source regions. The northern sources are the fold belt Caledonian and Hercynian metamorphic rocks that are widely exposed along the South China block and stacked with Mesozoic igneous rocks, and the southern sources are Mesozoic igneous rocks from the southern Panyu lower uplift. We analysed the characteristics of the provenance and sediment-dispersal patterns of the beach and bar systems in the Palaeogene third-order sequence framework on the basis of detritus, thin section, zircon and the geophysical response test data. The source and deposition areas were distinguished based on their palaeogeomorphology. The sedimentary material composition of the deposition area was determined based on the characteristics of the detrital assemblage and cathode luminescence, and the characteristics of the age distribution were determined in detail using detrital zircon U–Pb dating. This study suggests that the provenance system in the Palaeogene mainly consisted of Palaeozoic metamorphic rocks and Mesozoic igneous rocks, with a supplement of Proterozoic metamorphic rocks. The transport capacity of three large fault troughs that delivered the northern provenances gradually increased from the Wenchang Formation (E₂w) to the Enping Formation (E₃e), whereas the southern provenances were transported by four or five incised valleys in E₂w and then submerged in E₃e. In the 3D seismic area, the features of the beach and bar sedimentary systems were described and interpreted based an analysis of the well-based sedimentary facies, seismic reflection characteristics and multiple attribute clustering. The results show that the beach and bar systems by the short-axis braided deltas mainly developed in the upper member of E₂w and that the beach and bar systems on the subaqueous high in E₃e developed during the Palaeogene. In addition, the bedrock-beach bar sedimentary system in the lower member (E₃e^L) was transferred to the braided delta–beach bar sedimentary system in the upper member (E₃e^U).

© 2015 Elsevier Ltd. All rights reserved.

* Corresponding author. Faculty of Geoscience, State Key Laboratory of Petroleum Resources and Processing, China University of Petroleum, Beijing 102249, China.

** Corresponding author. Key Laboratory of Tectonics and Petroleum Resources, China University of Geosciences, Ministry of Education, Wuhan 430074, Hubei, China.

E-mail addresses: lqhckd@163.com (Q. Liu), zhuoscar@sohu.com (H. Zhu).

1. Introduction

The rifted lacustrine basins in the South China Sea (SCS) are characterized by multiple faults and subsidence centres and have undergone multiple tectonic activation episodes (Taylor and Hayes, 1983; Cullen et al., 2010; Franke, 2013; Franke et al., 2014; Sun et al., 2014; Zhou et al., 2014). Complex basin architectures are well documented as rifted basins developed within the coexistence of

multiple faults, uplifts and sags (Rosendahl, 1987; Morley et al., 1990; Schlische and Olsen, 1990; Schlische, 1991; Contreras et al., 1997; Gawthorpe and Leeder, 2000; Peacock et al., 2000; Henza et al., 2009; Schlische and Withjack, 2009). In addition, the proximal and multiple-sourced sediment supplies created distinctive patterns of multiple cycles, stages and depositional centres comprising diverse facies (Olsen, 1997; Gupta et al., 1998; Cope et al., 2010; Hsiao et al., 2010; Leeder, 2011; Masini et al., 2011). Gawthorpe and Leeder (2000) proposed a well-considered tectono-sedimentary model for active extensional basins and noted that the basin-fill architecture in a rift basin depends on a complex interaction among the three-dimensional (3-D) basement evolution through fault propagation, the evolution of drainages and drainage catchments, the effects of changing climate and base-level fluctuations. Sediment provenance analysis is an important tool for non-marine sedimentary basin analysis and is also helpful for identifying the essential elements of depositional systems including (1) sediment source areas, (2) source types and (3) sediment-transport pathways. These elements can aid in predicting the (1) palaeo-flow direction, (2) sedimentary facies distribution, (3) dispersal patterns of the depositional systems and (4) basin evolution history and palaeodepositional environment (Morton et al., 1991).

Conventional methods for sedimentary provenance analysis include heavy minerals (Blatt and Tooten, 1981), detrital component analysis (Dickinson, 1985; Roser and Korsch, 1988), pollen (Morton et al., 1991), fission-track thermochronology (Brandon and Garver, 1994) and geochemical and isotopic methods (Bhatia, 1983; Bonjour and Dabard, 1991; McLennan et al., 1993; Stevenson et al., 2000; Nemchin and Cawood, 2005; Miller et al., 2010), all of which require samples from either outcrops or cores. In the absence of rock samples, an alternative effective sedimentary provenance analysis approach using seismic and well data can be used (e.g., Wang et al., 2000; Zhao and Liu, 2003; Xu et al., 2007; Morley and Back, 2008).

Enping Sag is a hydrocarbon-rich region in the Pearl River Mouth Basin (PRMB) (Fig. 1a) (Liu et al., 2011), but the target layers are not yet well studied. Previous exploration has revealed that the Miocene Zhujiang Formation and the Oligocene Zhuhai Formation are the major reservoirs, followed by the Eocene Wenchang Formation and Oligocene Enping Formation, which are of secondary importance (Zhu and Mi, 2010). Despite the detailed documentation of the stratigraphy (Liu et al., 2013), sedimentology (Wang et al., 2011; Liu et al., 2015), tectonics (Wang et al., 2011) and petroleum exploration (Fu et al., 2007, 2009; Zhuo et al., 2007; Li et al., 2009; Wu et al., 2013), the petroleum geology of the Palaeogene is still not fully understood because of limited seismic and well data.

The South China fold system and Panyu lower uplift have been two important sediment sources since the Palaeogene (Fig. 1a). Previous investigations based on two-dimensional (2-D) seismic facies interpretation have suggested the presence of numerous fan deltas and braided deltas developed around the South China fold system and Panyu lower uplift (Lv et al., 2008; Wang et al., 2011). The Palaeogene sediments in the Enping sag were in fact mainly derived from the South China fold system and Panyu lower uplift. However, a detailed view of the influence of the uplifts and the spatial distribution of the sedimentary facies, especially beach and bar systems in the southern slope belt, is lacking because of poor provenance data and the lack of 3-D seismic data that cover the entire block.

In the study area, only six wells penetrate the interval of interest (Fig. 1b). Recently acquired 3-D seismic data (in-line and cross-line spacing of 25 m and 25 m, respectively), which cover the main Enping sag (with the area approximately 1800 km²), makes it possible to investigate the characteristics and diversity of the provenances between the South China fold system and the Panyu

lower uplift.

The primary objective of this study is to investigate the sediment provenance and sediment-dispersal patterns of the beach and bar systems using zircon provenance and 3-D seismic data. Specifically, this study seeks an (1) interpretation of the sediment-transport pathways and determination of the sediment source areas, (2) recognition of the prime material components in the sedimentary area through fragment composition and cathodoluminescence characteristics analyses, (3) identification of the sedimentary age provenance using zircon U–Pb dating, (4) documentation of the lateral lithological variations of the sand-prone and shale-prone areas, especially beach and bar systems, derived from well-based sedimentological characteristics, seismic facies and attributes and (5) the delineation of the planar distribution of the sedimentary facies for predicting the dispersal patterns of the beach and bar systems.

2. Geological setting and stratigraphy

As one of the largest marginal seas in the western Pacific, the South China Sea (SCS), which is located at the junction of the Eurasian, Pacific and Indian Ocean plates, has experienced a complicated tectonic and sedimentary evolutionary history (Briais et al., 1993; Gong et al., 1997; Sun et al., 2009). The Pearl River Mouth Basin (PRMB), located in the central part of the northern South China Sea margin, is one of the most important petroliferous basins in the entire region. The PRMB consists of five tectonic units; from south to north they are southern uplifted zone, southern depression zone, central uplifted zone, northern depression zone (including the Zhu-I and Zhu-III depressions) and northern uplifted zone (Fig. 1a). The basement of the PRMB consists of Jurassic and Cretaceous granites in its central and northern area, unmetamorphosed Mesozoic sedimentary rocks in the east and Palaeozoic quartzite and other metamorphic rocks in the west (Zhou et al., 2008).

The PRMB is an extensional basin on a continental margin. The evolution of the PRMB can be divided into an early faulting stage (the syn-rift stage) and a later subsiding stage (the post-rift stage) (Chen and Pei, 1993; Huang et al., 2003). During the syn-rift stage (56–30 Ma, Fig. 2), widespread crustal thinning and normal faulting accompanied by uplift and erosion contributed to the development of a series of grabens and half grabens along major NE and NW-trending fault sets (Chen and Pei, 1993; Li and Rao, 1994) (Fig. 1). Subsequently, the basin went into a postrift stage (30 Ma to the present, Fig. 2), which is divided by most investigators into two periods (e.g., Ru and Pigott, 1986; Su et al., 1989; Li and Rao, 1994; Chen, 2000). During the Late Oligocene to Middle Miocene, the basin was affected by extensional-shear and flower structures in the central area. After the Middle Miocene, tectonic movements were usually accompanied by extrusive volcanism that resulted in the large-scale hiatus of deposits and revival of faults.

The PRMB is a sedimentary system with terrestrial deposits followed by marine facies. Fig. 2 shows the generalized Cenozoic stratigraphy in the PRMB. The syn-rift sediments are composed of the Shenhu (E_{1s}), Wenchang (E_{2w}) and Enping (E_{3e}) Formations (Chen and Pei, 1993; Zhang et al., 2003; Zhu and Mi, 2010). The Shenhu Formation is dominated by red or mottled alluvial fan sands and conglomerates associated with volcanic sediments, which have little or no hydrocarbon-generating potential. The Wenchang Formation, which was deposited during the peak stage of lake expansion, mainly consists of grey to black organic-rich lacustrine shale interbedded with sandstone with a thickness of 1–2 km. The Enping Formation, which was deposited during the stage of lake regression, is dominated by fluvial-lacustrine-paludal shale, sandstone and thin coal beds with a thickness of

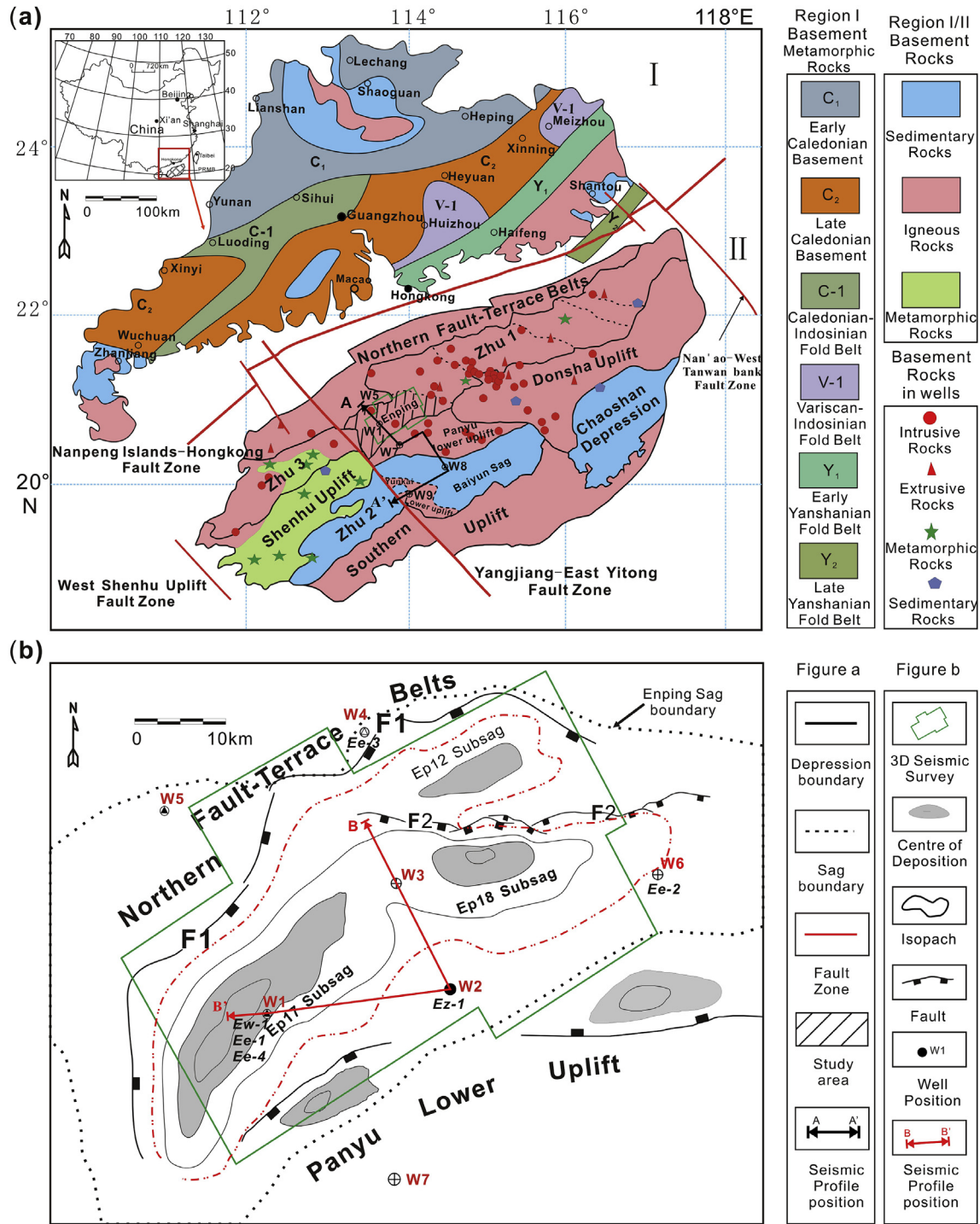


Fig. 1. Tectonic location and structure units characteristics of Enping sag, Pearl River Mouth Basin (PRMB). (a) Map shows the elementary structural features and basement of the PRMB (Guangdong Province Bureau of Geology and Mineral Resources (1988); China geological Atlas of editorial board, 2002; Li and Li, 2007; Zhang, 2008; Zhang et al., 2009; Zhang et al., 2013; Yan et al., 2014) and (b) the main morphological pattern of the Enping sag. The black line A–A' represent seismic lines used in Fig. 6 and red line B–B' represent seismic lines used in Fig. 14.

1100–1600 m. The major source rocks in the PRMB mainly developed during the deposition of the Wenchang Formation and Enping Formation (Chen and Pei, 1993; Dai and Pang, 1999; Zhu et al., 1999; Jiang and Yang, 2000). The postrift sediments consist of Zhuhai (E_{3Z}), Zhujiang (N_{1Z}), Hanjiang (N_{1h}), Yuehai (N_{1Y}) and Wanshan (N_{2w}) Formations and Quaternary sediments (Fig. 2). These strata constitute a good vertical ascending source/reservoir/seal rock

assemblage.

The Enping sag is situated in the Zhu I Depression, which is the central part of the northern continental shelf in the Pearl River Mouth Basin (Fig. 1a). The Nan Peng-Hong Kong Fault Zone divides the regional basement lithology. The northern basement rocks (region I in Fig. 1a) are the fold belt Caledonian and Hercynian metamorphic rocks that are widely exposed along the South China

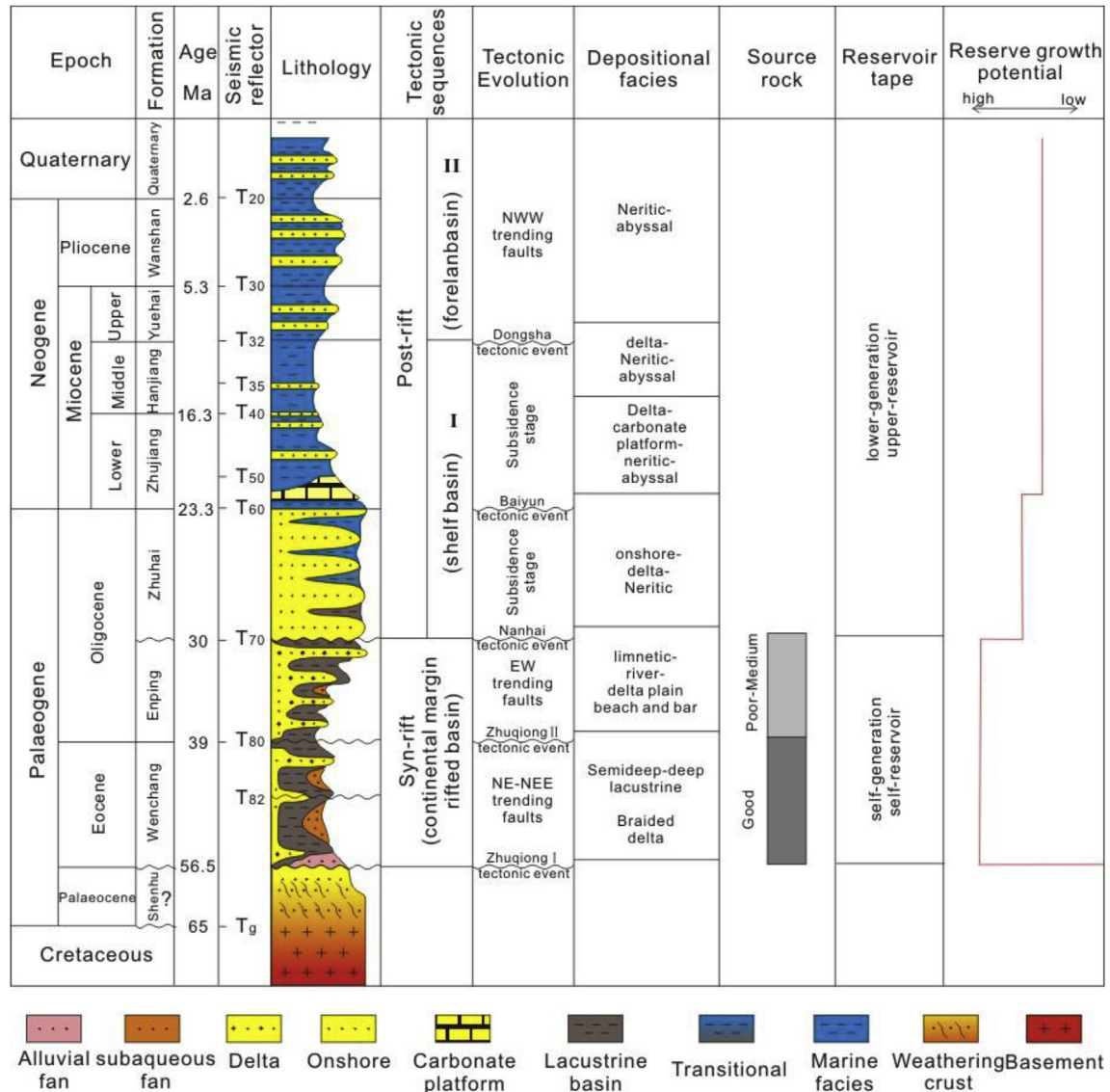


Fig. 2. Generalized stratigraphic column of the Pearl River Mouth Basin showing lithologies, tectonic evolution, depositional facies and source-reservoir-cap assemblages (after Zhang et al., 2003; Zhu and Mi, 2010; Liu et al., 2015). The study interval is the Eocene Wenchang and Oligocene Enping Formations, which were deposited in the syn-rift stage.

block and stacked with Mesozoic igneous rocks (145–250 Ma) (Guangdong Province Bureau of Geology and Mineral Resources (1988); Huang, 1989; Li, 2000; China geological Atlas of editorial board, 2002; Li and Li, 2007; Zhang, 2008; Zhang et al., 2009; Xu et al., 2009). In the southern part (region II in Fig. 1a), the Panyu lower uplift is composed of Mesozoic igneous rocks (absolute ages between 70.5 and 153 ± 6.0 Ma, as measured by K–Ar, Rb–Sr isochron and U–Pb zircon analyses) (Li et al., 1998; Lu et al., 2011; Zhang et al., 2013; Yan et al., 2014). As a whole, these pre-Tertiary basements are components of the southern and northern provenance systems in the Palaeogene of the Enping Sag.

The Zhuqiong Event continued from the Palaeocene (Zhuqiong I) to the Late Eocene (Zhuqiong II) and spanned the rifting of the Enping sag (Pang et al., 2008). Under the control of the Zhuqiong movement, the sag transformed from rifted (Wenchang Formation) to rift and depression transition (Enping Formation) with stabilized uplift-erosion, especially accompanied by fault and magmatic activity. During the depositional period of the Enping Formation, the northern fault-terrace belts and Panyu lower uplift continued to

subside and formed subaqueous highs, whereas the lake continued to expand quickly and covered almost the entire sag (Mi et al., 2008; Wang et al., 2011; Liu et al., 2015). In the Palaeogene, the deposition in the Enping sag was distributed along a NEE-SWW trend and was dominated by syn-faults (F1 and F2 shown in Fig. 1b). Overall, the South China fold belts in the north acted as a regional provenance system (region I), and the Mesozoic igneous basement of Panyu lower uplift acted as a local provenance system (region II) in the south.

Using W1 in the Wenchang Formation and six wells (W1–W6) in the Enping Formation (Fig. 1b) and an integrated analysis of the regional tectonics, dynamic mechanisms, termination patterns of seismic reflection events, lithology and log data, palaeontology and paleoenvironmental data, the Eocene Wenchang (E_{2w}) Formation can be divided into two sub-second-order (lower and upper members of E_{2w} Formation) and six third-order sequences (Liu et al., 2013), and the Oligocene Enping (E_{3e}) Formation can be divided into three third-order sequences (Liu et al., 2015) (Fig. 3).

The poor continuity of the seismic reflections, rapid variations in

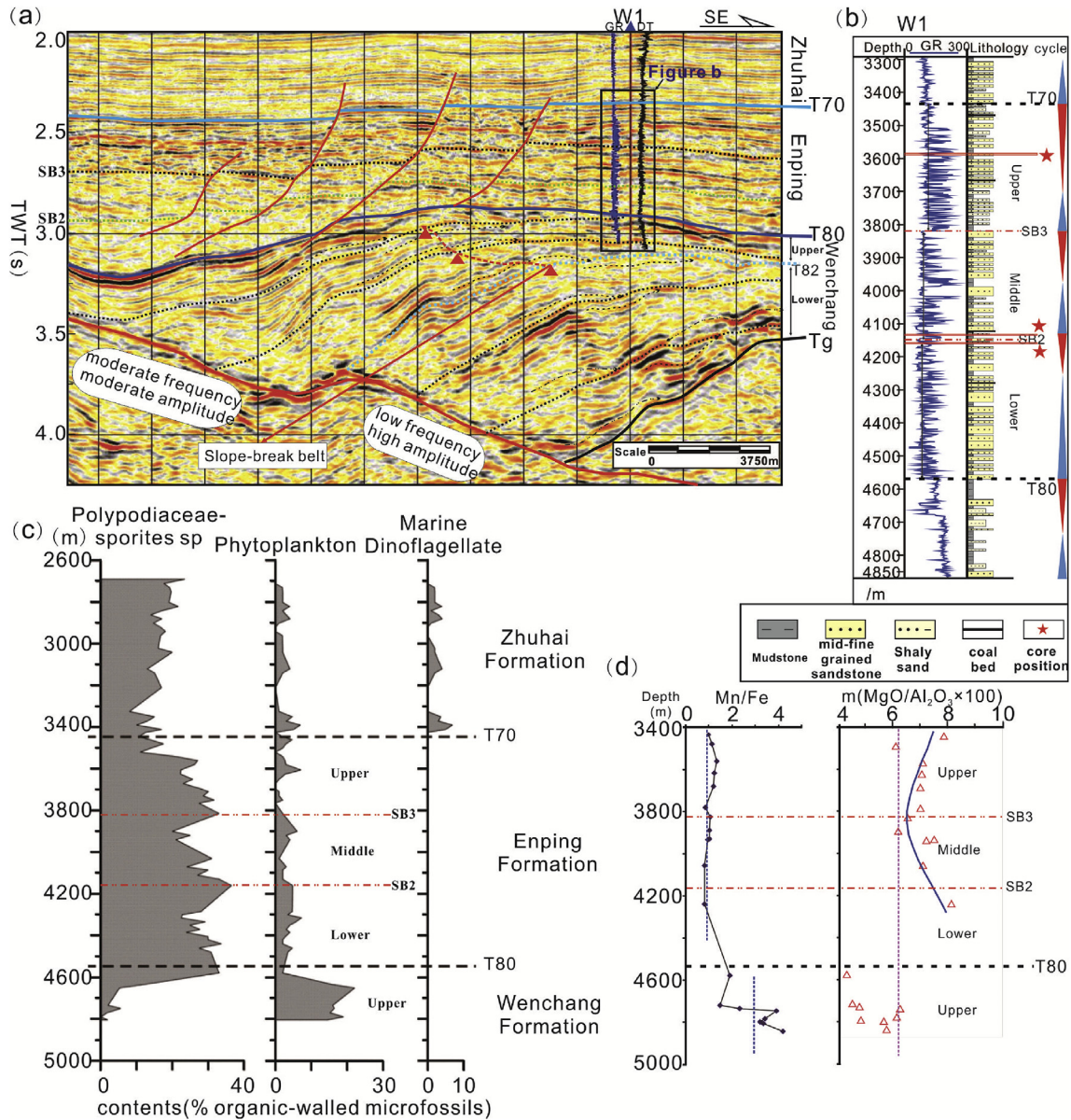


Fig. 3. Generalized stratigraphic units of the study interval, the Eocene Wenchang and Oligocene Enping Formations, showing (a) seismic reflections and a logging curve (W1), (b) lithology and depositional sequence (the location of W1 is shown in Fig. 3a), (c) palaeontology (content of Polyodiaceae-sporites sp, Phytoplankton and marine Dinoflagellates), (d) relative palaeobathymetric curves (ratios of Mn/Fe and $m(\text{MgO}/\text{Al}_2\text{O}_3 \times 100)$) and sequence stratigraphic framework associations. The red pentagrams in Fig. 3b represent the core positions used in Fig. 10.

the seismic amplitude and the presence of a few wedge-shaped chaotic seismic reflections (Fig. 3a) adjacent to syndimentary faults (F1, F2) in the northern steep slope zone reveal effects related to the Zhuqiong movement (Wang et al., 2011). The upper member of the Wenchang Formation (E_2w^U) predominantly consists of multistory mudstone or calcareous mudstone intercalated with thin siltstone beds (Fig. 3b). The debris (well W1 block) appears as grey to black, phytoplankton extensively developed (Fig. 3c), and the higher ratios of Mn/Fe (3–4) and lower ratios of m ($\text{MgO}/\text{Al}_2\text{O}_3 \times 100$) (4–5) (Fig. 3d) indicate a semi-deep lacustrine environment. Nevertheless, the Enping Formation is primarily composed of thick sandy conglomerate, pebbly fine-middle sand with thin layers of siltstone and mudstone (Fig. 3b). The debris appears as greyish white, with fewer phytoplankton (Fig. 3c), lower ratios of Mn/Fe (approximately 1) and higher ratios of m (6–8) (Fig. 3d) that imply a shallow lacustrine environment. The Gamma

Ray (GR) curve is mainly box-shaped with high amplitudes and few funnel-shaped features, which can be interpreted as braided channels, subaqueous distributary channels and a few mouth bars. The sedimentary environment of the E_3e Formation is related to large shallow braided delta deposits in the shore and shallow lake environment (Wang et al., 2011; Xue, 2013). Meanwhile, the southern lower uplift (e.g., the W2 block), which has low dips and a subdued topography that were beneficial for beach and bar deposits, was broader and shallower (Liu et al., 2015; Zeng et al., 2015).

3. Provenance analysis

The tectonic framework and palaeogeomorphology of the Sag (Enping Sag) can be used to analyse the depositional centre, obtain the sediment-transport pathways and depositional area, and

provide the macroscopic direction of the provenance system (Lin et al., 2004; Deng et al., 2008). Based on the palaeogeomorphology of the depositional stages of the Wenchang and Enping Formations, we analysed the sandstone fragment compositions from the Enping sag, Panyu lower uplift, Baiyun sag to the Yunkai lower uplift, using wells W1, W8 and W9. Using the zircon U–Pb ages from the wells (W1, W2, W4 and W6), the semi-quantitative provenance direction of the Enping sag in the Palaeogene was determined.

3.1. Palaeogeomorphological features

Sediment distribution in a source-to-sink system corresponds to 'the sediment routing system' (Allen, 2005, 2008a, b; Sømme et al., 2009), which is often described as the dynamic processes and feedback mechanisms that govern sediment dispersal in erosional-depositional systems (Allen and Hovius, 1998; Arribas et al., 2000; Critelli et al., 1995, 1997; Densmore et al., 2007; Sømme et al., 2013; Sømme and Jackson, 2013; Prizomwala et al., 2014). The evolution of this system is reflected by morphological modifications within one or several adjacent segments (Sømme et al., 2009); thus palaeogeomorphological research is an effective method to understand and predict the sedimentary facies and dispersal patterns of depositional systems (Martin, 1966; Richards et al., 1998; Zeng and Hentz, 2004; Posamentier, 2004; Posamentier et al., 2007; Masini et al., 2011; Dumont et al., 2012; Zhu et al., 2014a, 2014b).

The palaeogeomorphological architecture of the study area is dominated by the Panyu lower uplift, South China fold belts and NE–or ENE-trending boundary fault sets. The topographic features seen on the map include fault-troughs, incised-valleys, hills (A, B, C, D and E zones in the north and the F zone in the south), slope belts and sinks (Figs. 4 and 5). The subsags in the Enping Sag (Ep17 subsag, Ep18 subsag and Ep12 subsag) were not connected at the time of the deposition of the Wenchang Formation (Fig. 4a) and generally were connected for the Enping Formation (Fig. 5a).

3.1.1. Faulted-trough sediment-transport pathways

The South China fold belts, which are mainly composed of metamorphic rocks and granite, had transformed from eroded uplifted land to peneplain landforms (Davis, 1889) during the depositional times of the Eocene Wenchang and Oligocene Enping Formations (Figs. 4–5). During the syn-rift stage, strong erosion in

the northern section contributed to a high transport capacity corresponding to widely distributed fan sand bodies along the Syngenetic Fault (Syn-Fault) F1 and Fault F2 in the depositional area. As a result of tectonic movement (Zhuqiong I and Zhuqiong II), faults in northern section are abundant and steep in the sag. Three large-scale, ESE-trending and far-extended faults are accompanied by three faulted-trough sediment-transport pathways (I, II and III) in the northern fault-terrace belts. Four SW-trending faulted-trough sediment-transport pathways (IV, V, VI and VII) in the E zone are controlled by syn-fault F2 (Figs. 4a and 5a).

Pathway I is located between zone A and zone B and has a maximum settlement of 1712 m in the northern fault-terrace belts (Fig. 5b). The source area with strong erosion appears to be at the intersection of two major double-faulted troughs characterized by parallel and subparallel seismic reflections (Fig. 5b). The deposits in the faulted troughs parallel to the sediment-transport direction exhibit multiple distinctive large-scale progradational seismic reflections.

Pathway II is located between zone B and zone C, and its topography is the secondary settlement (approximately 1104 m) (Fig. 5c). In the depositional area, pathway II can be divided into two faulted-trough sediment-transport pathways (II₁ and II₂) in the SSE or SE directions under the control of syn-fault F1 (Fig. 4b). The deposits, with some small-scale progradational or chaotic seismic reflections, are seen at the foot of the bounding faults near the margin of syn-fault F1 (Fig. 3a).

Pathway III is located between zone C and zone D, with a minimum settlement of 811 m in the northern fault-terrace belts (Fig. 5d). In the depositional area, pathway III merged three faulted-trough sediment-transport pathways (III₁, III₂ and III₃) along S-, SE- or ESE trends (Fig. 4b).

Pathways IV, V, VI and VII are faulted troughs that are characterized by wedge-shaped and chaotic channel-fill seismic reflections, with smaller width-depth ratios and lower delivering capabilities during the depositional period of the Wenchang Formation and the lower and middle member of the Enping Formation (Fig. 4c). The sediments are indicated by small-scale chaotic seismic reflections at the feet of the bounding faults near the margin of syn-fault F2 (Wang et al., 2011; Liu, 2013).

3.1.2. Incised-valley sediment-transport pathways

The southern lower uplift (zone F), which is mainly composed of

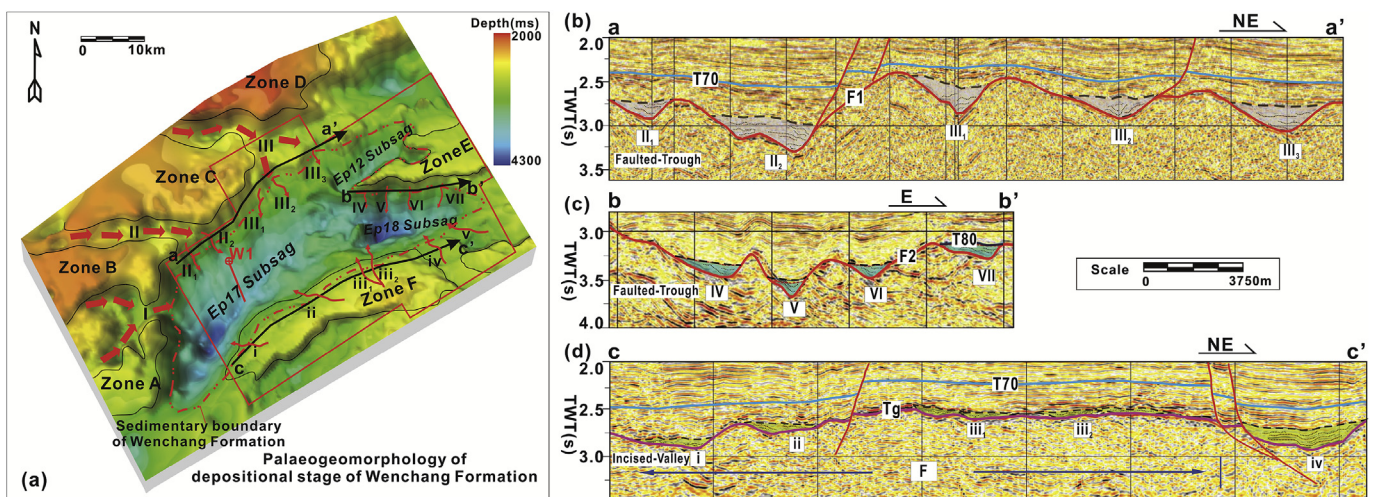


Fig. 4. (a) Palaeogeomorphology of depositional stage of Wenchang Formation showing the tectonic units and sediment transfer pathway, (b) seismic profile showing the fault-trough sediment-transport pathways along the syngenetic fault F1, (c) seismic profile showing the fault-trough sediment-transport pathways along the syngenetic fault F2, (d) seismic profile showing the incised-valley sediment-transport pathways in the southern lower uplift.

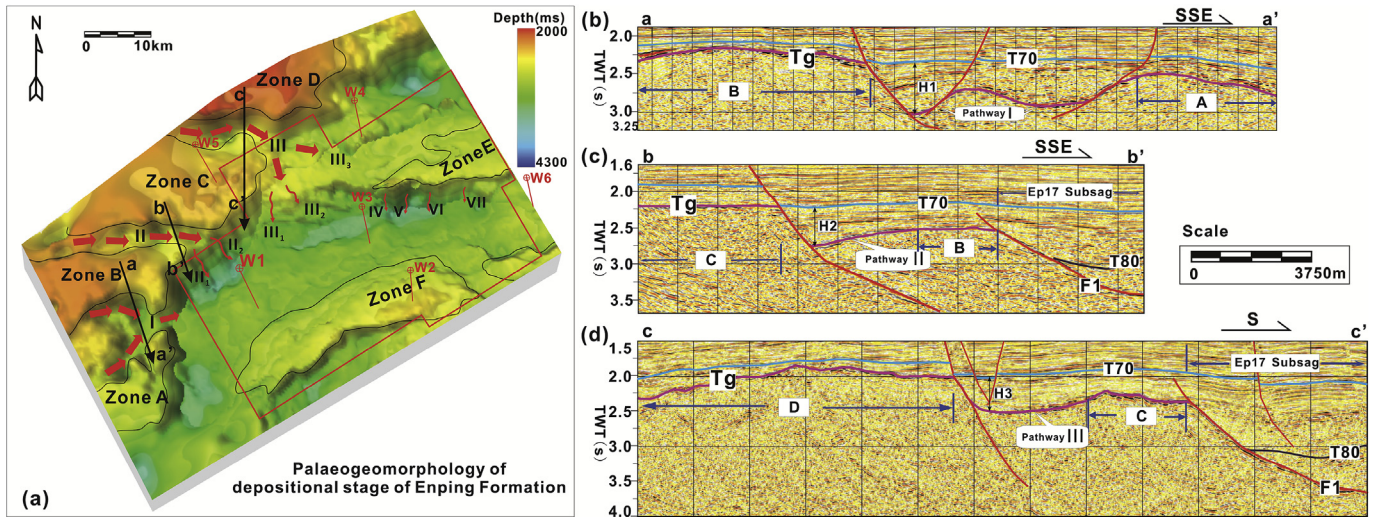


Fig. 5. (a) palaeogeomorphology of depositional stage of Enping Formation, (b) seismic profile showing the fault-trough sediment-transport pathway I in the northern fault-terrace belts, (c) seismic profile showing the fault-trough sediment-transport pathway II in the northern fault-terrace belts, (d) seismic profile showing the fault-trough sediment-transport pathway III in the northern fault-terrace belts.

granite, has a stable tectonic activity, low dip and subdued topography (Figs. 4a and 5a). Weak erosion in the southern section led to a much more limited sediment supply of rock fragments with predominant quartz grains. Four or five migrated incised-valleys (i, ii, iii₁, iii₂ and iv) with smaller width-depth ratios and lower delivering capabilities are controlled by the palaeogeomorphology of the southern slope break zone (Fig. 4a and d). The width-depth ratios of these valleys gradually decreased downstream. These incised-valleys were used to determine the sediment-transport direction and the sedimentary dispersal system of the Wenchang Formation and are perceived as potential high-quality reservoirs in the Enping Formation.

3.2. Sandstone detrital compositions

Because quartz is the most common and stable mineral in the Earth, it is one of the most extensively studied minerals. In spite of the simple composition of quartz, its deformation microstructures and fabrics display considerable complexity (Critelli et al., 2008; Haddad et al., 2006; Perri et al., 2011, 2013). According to the different compositions of the basement rocks in the northern and southern source areas (Li and Li, 2007; Zhang et al., 2013; Yan et al., 2014), the fragment content in detritus can be used to trace the proximal sources and to indicate the transport distances of the source rocks.

We selected the cross-well dip seismic section A–A' (shown in Fig. 1a) from the Enping sag, Panyu lower uplift and Baiyun sag to Yunkai lower uplift, with wells W1, W8 and W9 (Fig. 6), depending upon the distribution of the wells that drilled to the pre-Cenozoic and basement lithologies (Li et al., 1998; Lu et al., 2011; Sun et al., 2014). During the depositional period of the Wenchang Formation, the Enping sag and Baiyun sag, which are separated by the Panyu lower uplift (Fig. 6a), were not interconnected. Their interconnection began after the Zhuqiong II movement (Fig. 6a). The depositional patterns of the southern lower uplift (F zone) were dominated by the northern South China fold belts and the southern Panyu lower uplift in the Enping Formation. Furthermore, the source of the Baiyun sag is represented by the intermediate-felsic volcanic rocks and granites in the South China fold system (Yanshanian Fold Belt in Fig. 1a) and ancient sedimentary-metamorphic rocks, which were carried by the ancient Pearl River in the South

China inlands subsequent to the beginning of the Zhujiang Period (Liu et al., 2013).

Point counting was performed on these sandstones following the sandstone classification of Folk (1974). The Enping Formation sandstone samples are lithic quartz sandstones and contain quartz (Q) in the range 64.2–89.7%, 2.5–28.3% feldspar (F) and 7.8–25.6% rock fragment (R). A similar result was obtained by Zhuo et al. (2007) for 36 Enping Formation sandstone samples (see Fig. 6b). The stable detritus component mainly consists of metamorphic and igneous fragments with few sedimentary fragments (<15%) in the Enping Formation. In more detail, the metamorphic fragment content of W1 (9 samples), which was quantified by pointcounting, increased from 42.6% (E_3e^L) to 55.4% (E_3e^U), whereas the igneous fragment content remained stable in the Enping Sag. In the Baiyun sag, the metamorphic fragment content of W8 (10 samples) increased gradually from 38.2% (E_3e^L) to 50.2% (E_3e^U) in the Enping Formation. Furthermore, the metamorphic fragment content of W1 (Enping sag) was 55.4% in the upper member of Enping Formation, decreased to 50.2% in W8 (Baiyun sag) and finally decreased to 12.3% in W9 (Yunkai lower uplift).

The fragment composition of W1 indicates that the sediments were supplied by the South China fold belts (region I) (Guangdong Province Bureau of Geology and Mineral Resources (1988); China geological Atlas of editorial board, 2002) along the faulted-trough sediment-transport pathways (II₁ and II₂). In the E_3e^U stage, the transport capacity of regional provenance (region I) gradually increased and migrated from the Enping sag to the Baiyun sag.

The cathodoluminescence imaging data from the Enping Formation in wells W1 (EP17 subsag), W6 (EP18 subsag) and W4 (EP12 subsag) provided additional information that was used to interpret provenance (Fig. 7). The quartz fragment is predominantly light blue-purple (E_3e^L , E_3e^M) to brown (E_3e^U) under the excitation of the cathode ray, which means that the quartz was cooled from high temperatures and that the source rocks were principally composed of volcanic, plutonic or metamorphic rocks (Hunt, 2013; Frelinger et al., 2015). The feldspars are mainly light blue (E_3e^L and E_3e^M), with a few yellow green (E_3e^U) (Fig. 7), which indicates that potassium feldspar is the primary type of feldspar (Omer and Friis, 2014). The cathode ray features of the detrital quartz and feldspar further illustrate that the source rocks were magmatic and metamorphic rocks (mainly in region I).

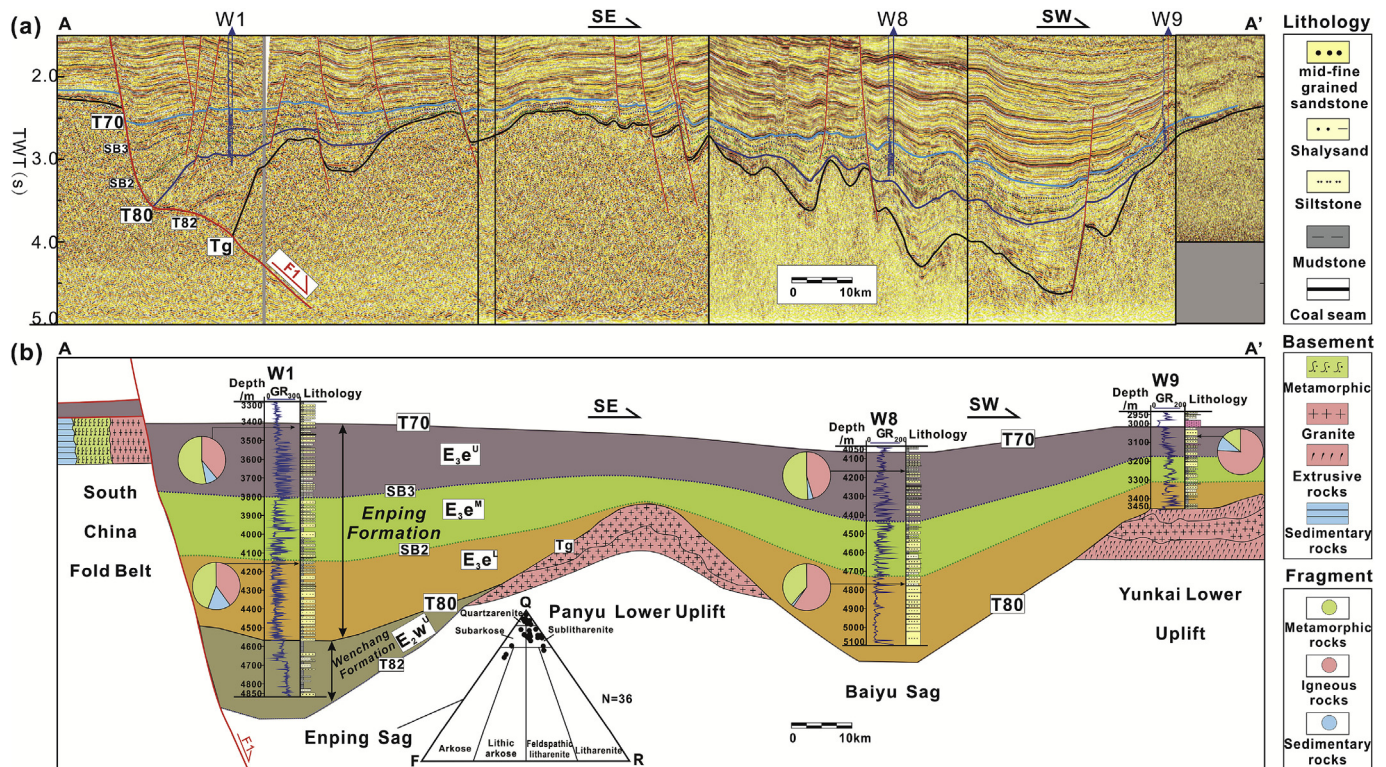


Fig. 6. Cross-well dip seismic section A–A' showing (a) regional stratigraphic correlation seismic profile of the Palaeogene from the Enping sag, Panyu lower uplift to Baiyu sag; (b) sequence stratigraphic correlation section from W1, W8 to W9 including the rock fragments composition in the Enping Formation.

3.3. Detrital zircon U–Pb ages

The detrital-zircon U–Pb geochronology dating method is a highly precise technical method used in modern chronostratigraphic studies and the quantitative analysis of sedimentary provenance in clastics rock.

3.3.1. Samples and methods

Six samples for detrital zircon analysis from each formation (E_2w^U , E_3e^L , E_3e^M , E_3e^U and E_3z) were collected and named Ew-1, Ee-1, Ee-2, Ee-3, Ee-4 and Ez-1 (Fig. 1b). Three of the samples (Ew-1, Ee-1 and Ee-4) were obtained near the Enping main depression, Ee-3 was obtained near the northern fault-terrace belts, and Ee-2 and Ez-1 were collected near the southern lower uplift. The sampled sections are located in the Enping sag, north-western Zhu I depression, central Pearl River Mouth Basin (PRMB). All of the samples were sandstone, except for two fine-grained samples (Ew-1 and Ez-1).

The zircons were separated using conventional heavy liquid and magnetic techniques. The grains were selected under a binocular microscope and mounted in epoxy resin, sectioned approximately in half and polished. The CL images were made using a JEOL JXA-8100 electron microprobe and were used to decipher the internal structures of the sectioned grains and to avoid areas with potentially high common lead content, such as inclusions, fractures and metamict structures.

Zircon U–Pb dating was conducted on the LA-ICP-MS at the State Key Laboratory of Geological Processes and Mineral Resources, China University of Geosciences at Wuhan. The performance of the instrument and its detailed analytical procedures were described by Zong et al. (2010). A pulsed 193 nm Geolas 2005M laser-ablation system coupled to an Agilent 7500 ICP-MS was used for the data collection. The laser spot size was $\sim 32 \mu\text{m}$,

and a repetition rate of 6 Hz was used for the U–Pb data acquisition. The sample data used in each analysis were comprised of an approximately 20 s background acquisition (gas blank) followed by a 50 s data acquisition. All of the measurements were normalized relative to standard zircons 91500 and GJ-1. Standard silicate glass NIST SRM610 was used to calibrate the contents of the trace elements. The off-line selection and integration of the background and analysis signals and time-drift correction and quantitative calibration were performed using ICPMS-DataCal (Liu et al., 2008). The U–Pb ages were calculated using ISOPLOT 3.00 (Ludwig, 2003). Our measurements of GJ-1 and 91500 yielded weighted mean $^{206}\text{Pb}/^{238}\text{U}$ ages of $599.9 \pm 1.8 \text{ Ma}$ (2σ , MSWD = 0.045, $n = 40$) and $1062.4 \pm 1.6 \text{ Ma}$ (2σ , MSWD = 0.0016, $n = 206$), respectively, which are in good agreement with the apparent ID-TIMS $^{206}\text{Pb}/^{238}\text{U}$ ages of 598.5–602.7 Ma and $1062.4 \pm 0.4 (2\sigma)$ (Jackson et al., 2004).

3.3.2. Zircon U–Pb LA-ICP-MS analytical results

In the depositional area, six samples of detrital zircon U–Pb ages were dated, and their ages ranged from 2498 ± 33 to $99 \pm 2 \text{ Ma}$, with a multi-spiked probability density curve (Figs. 8–10).

3.3.2.1. Description

1) E_2w^U

During the depositional period of E_2w^U , the provenance of the detritus drilled in W1 (located at the southern slope-break belt and coupled with the north-trending progradational seismic reflections in Fig. 3a) was mainly from the southern lower uplift (Lv et al., 2008; Wang et al., 2011). Sample Ew-1, which came from E_2w^U , was from a grey argillaceous sandstone. A total of 27 grains yielded ages with a concordance >90% and are plotted on a probability density diagram (Fig. 8). These zircons yielded ages ranging from $1651 \pm 12 \text{ Ma}$

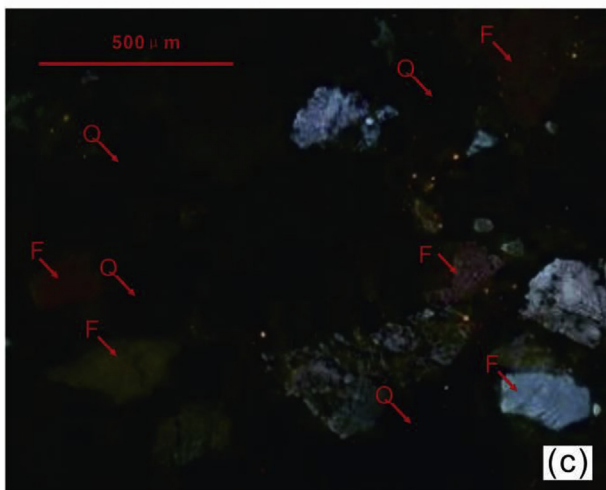
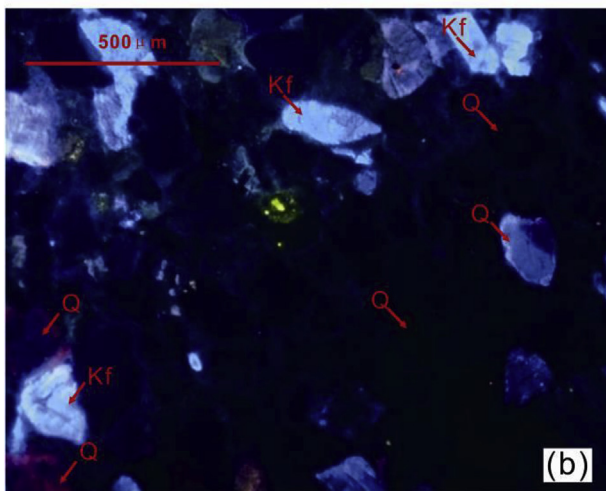
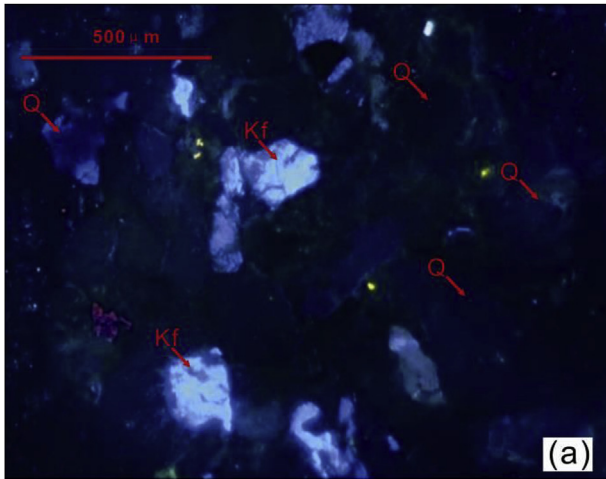


Fig. 7. Cathodoluminescence images of sandstones from the Palaeogene in the Enping Sag. (a) Thin section at 4153.8 m MD in W1 (E_3e^L) showing blue-purple quartz clasts. (b) Thin section at 3676.6 m MD in W6 (E_3e^M) showing blue-purple quartz clasts and bright blue potash feldspar. (c) Thin section at 3640.0 m MD in W4 (E_3e^U) showing brown quartz clasts and yellowish green plagioclase.

to 148 ± 2 Ma. They can be classified into two groups; the dominant group has an age of 169–148 Ma (Mesozoic) and contains 82.1% grains, whereas the second group with ages from 448 to 252 Ma

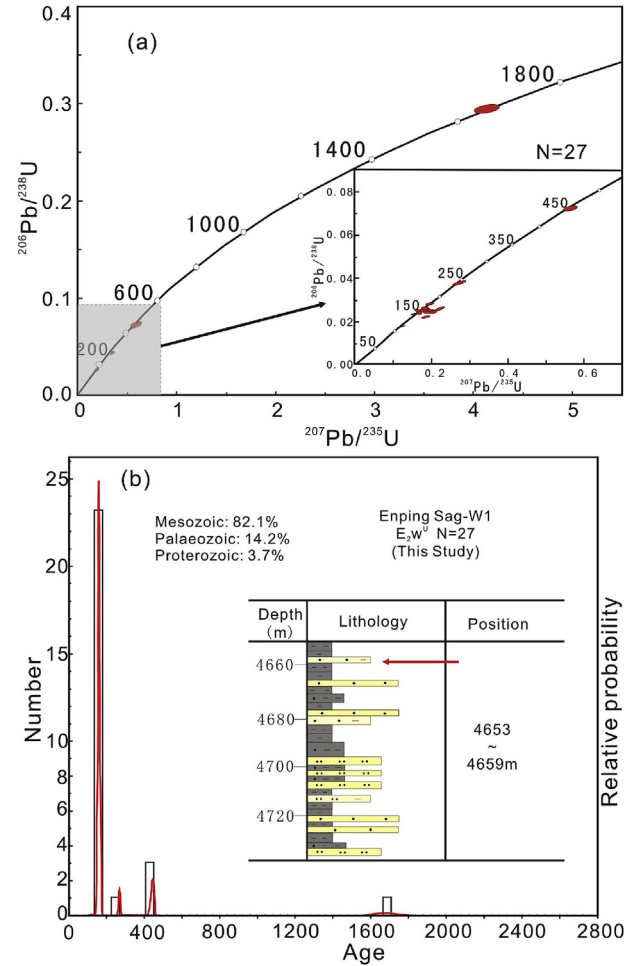


Fig. 8. Representative Concordia diagram (a) and histogram with probability density curve (b) of the detrital zircon U–Pb ages for the argillaceous sandstone from W1 (E_2w^U), Upper member of the Wenchang Formation (E_2w^U), Enping sag.

(Palaeozoic) is less represented, with three grains approximately 436 Ma. In addition, an isolated grain of Proterozoic age (1665 Ma) was found (Fig. 8b).

2) E_3e

Sample Ee-1, which came from E_3e^L , was from a greyish white middle-grained sandstone. A total of 22 analyses with a concordance of >90% are shown in a probability density diagram (Fig. 9a). The ages range from 1750 ± 54 Ma to 143 ± 2 Ma and fall into three groups: 166–143 Ma (Mesozoic), with a peak at 161 Ma, 387–245 Ma (Neopalaeozoic), with a peak (or mean) at 263 Ma, and 568–420 Ma (Eopalaeozoic), with a peak at 437 Ma. In addition, there are two separated Proterozoic peaks at 965 Ma and 1750 Ma (Fig. 9b). Palaeozoic zircon dominates and comprises 59.1% of the grains, unlike sample Ew-1.

Sample Ee-2, which came from E_3e^M , was collected from a greyish white fine-grained sandstone. The analysed grains yielded three major age groups (Mesozoic, Palaeozoic and Proterozoic) from 33 data points (Fig. 9c). The ages range from 963 ± 14 Ma to 99 ± 2 Ma and predominantly range from 452 to 416 Ma (Eopalaeozoic) (Fig. 9d).

Sample Ee-3, which came from E_3e^U , was from a greyish white middle-grained sandstone. A total of 28 data analyses produced ages ranging from 2101 ± 49 Ma to 143 ± 2 Ma (Fig. 9e). The ages

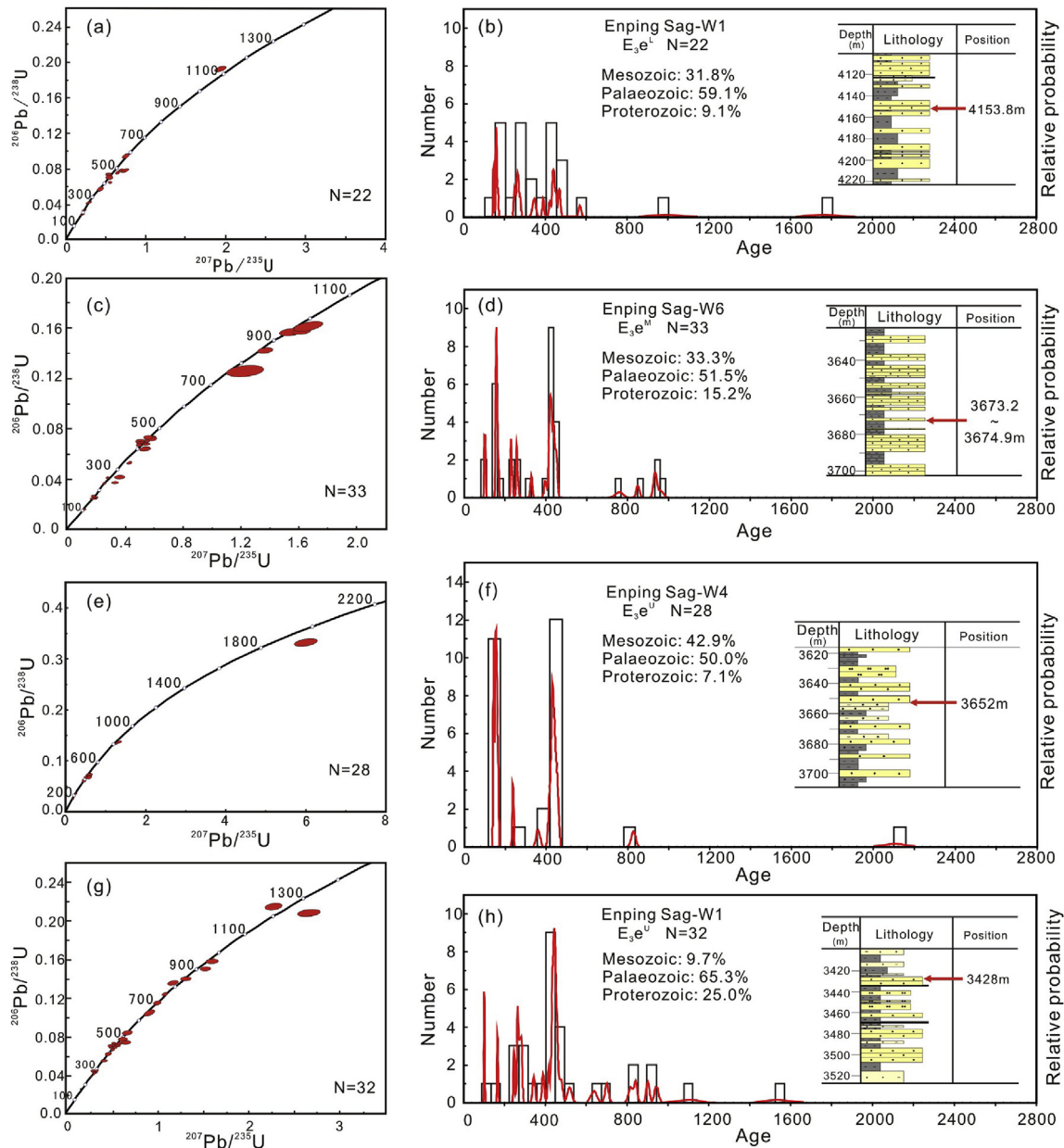


Fig. 9. Representative Concordia diagrams (a, c, e, g) and relative probability plots (b, d, f, h) of the detrital zircon U–Pb ages for the middle–fine sandstone samples W1 (Ee-1, Ee-4), W6 (Ee-2) and W4 (Ee-3) from the Enping Formation, Enping sag.

were grouped into three regions, and the 458–414 Ma group (Eopalaeozoic) was dominant, akin to sample Ee-1 (Fig. 9f).

Sample Ee-4, which came from E₃e^U, was from a greyish white middle-grained sandstone. A total of 32 data points fall into three groups and are plotted on a probability density diagram (Fig. 9g). The proportion of 246–102 Ma (Mesozoic) decreased to 9.7%; the dominant groups are 389–264 Ma (Neopalaeozoic) and 519–416 Ma (Eopalaeozoic) with 65.3% grains. A further group is at 1533–638 Ma (Proterozoic) with 25.0% grains (Fig. 9h).

3) E₃z

Sample Ez-1 is from a grey–greyish white argillaceous sandstone in E₃z. A total of 34 analyses produced ages ranging from 2498 ± 33 Ma to 117 ± 2 Ma (Fig. 10a). The ages were grouped into four populations, with a new age cluster with a range of

2502–2607 Ma (Archaeozoic). Palaeozoic zircon dominates and comprises 44.1% of the grains. There are two separated Proterozoic peaks at 979 Ma and 1953 Ma. (Fig. 10b).

3.3.2.2. Interpretation. By comparing the detrital zircon ages from the Enping Sag with time equivalent data from the South China block and the Pearl River Mouth basin basement, it is clear that the provenance features in the Palaeogene Enping sag varied. Specifically, the single source of Mesozoic igneous grains derived from the basement of the southern Panyu lower uplift in E₂w^U evolved to a mixed provenance of Palaeozoic metamorphic, Mesozoic igneous and a few Proterozoic metamorphic grains from the basement of the South China fold belts and the Panyu lower uplift in E₃e. They finally transformed to predominantly metamorphic grains associated with the South China fold belts in the Zhuhai Formation (E₃z). Generally, the proportion of Palaeozoic and Proterozoic

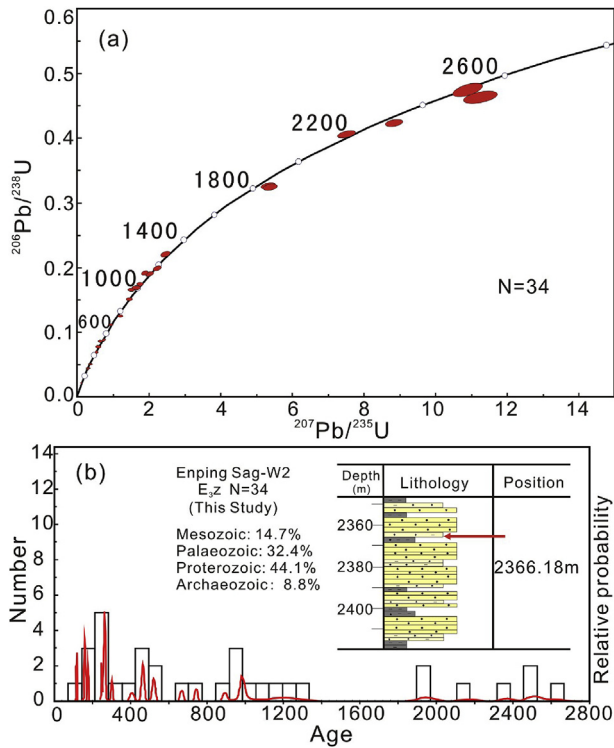


Fig. 10. Representative Concordia diagram (a) and histogram with probability density curve (b) of the detrital zircon U–Pb ages for the argillaceous sandstone from W2 (Ez-1), Zhuhai Formation, Enping sag.

metamorphic grains increased gradually from the base (E_3e^L) to the top (E_3e^U) in the Enping Formation, whereas the Mesozoic igneous grains decreased.

4. Sedimentary facies analysis

Based on the relationship of the sediment-transport pathways and sedimentary unloading area, we applied seismic sedimentology to the entire block covered by 3-D seismic survey to extend the well data study and to provide a more detailed mapping of the sedimentary facies.

4.1. Well-based facies analysis

In this study, two major facies, a braided delta (deltaic front and plain) facies and a beach-bar facies, were identified on the basis of lithology, sedimentary structures (Fig. 11), wireline log patterns (Fig. 3b) and facies successions. The key observations and process-based interpretations are outlined below.

4.1.1. Braided delta facies

4.1.1.1. Description. The braided delta facies, which were deposited in the southwestern Enping Sag near the depocenter (W1 block), are characterized by fine-grained sandstone, silty sandstone and pebble sandstone, intercalated with thin-bedded mudstone and multiple coal beds (Fig. 3b). The sandstone in W1 is light grey to grey and moderately sorted, commonly forming fining-upward successions (0.01 m–1 m) (Fig. 11 a–d) and a few coarsening-upward successions (Fig. 11e) in the cores. Fine and medium interbedded sandstones with wedge-shaped (Fig. 11a) and slumped beddings (Fig. 11d) are common at the top of the fining-upward successions, whereas medium and coarse interbedded sandstones are common at the bottom with locally scattered pebbles and

erosional bases (Fig. 11 a–c). In the GR logs, this facies generally shows a box-shaped pattern with medium–high peak values and few funnel-shaped patterns (Fig. 3b).

4.1.1.2. Interpretation. According to its distribution (Fig. 5a), relative palaeowater depth (Fig. 3d), lithology and sedimentary structures (Fig. 11), this facies is considered to be a shallow-water braided delta, as suggested by Wang et al. (2011) and Liu et al. (2015). In the E_3e^U stage, fining-upward conglomeratic sandstones and parallel to cross-bedded coarse-grained to fine-grained sandstones with erosional bases are interpreted as distributary channel deposits in a shallow-water delta plain (Fig. 11 a–c). In the E_3e^M and E_3e^L stages, the grey sandstones with tabular cross-bedding and trough cross-bedding are interpreted as distal mouth bar, mouth bar and distributary channel deposits in the deltaic front (Fig. 11 d–e).

4.1.2. Beach and bar facies

4.1.2.1. Description. The beach and bar facies deposited in the southern lower uplift zone (well W2 block) are mainly comprised of fine-grained sandstone, medium sandstone, pebbly sandstone and a small amount of conglomerate (Liu et al., 2015). A single sandstone layer of sandy or gravelly beach-bar ranges from 2 to 8 m. At the top of the Enping Formation, the sedimentary structures of the sandy beach and bar facies include wedge-shaped cross-bedding and micro-wavy bedding (Fig. 11f) in the cores. The sandy beach and bar facies (E_3e^U) shows funnel-shaped or box-shaped GR log curves (Liu et al., 2015). At the bottom of the Enping Formation, the gravels are well-rounded with grain sizes ranging from 2 to 20 mm (Fig. 11g). The observed sedimentary structures in the gravelly beach and bar facies include massive bedding and graded bedding (Fig. 11g). In the GR log curves, the gravelly beach and bar facies (E_3e^L) presents tooth-like box-shapes or funnel-shape patterns (Liu et al., 2015).

4.1.2.2. Interpretation. During the deposition of E_3e^U , the well-sorted and well-rounded fine-grained sediments are interpreted as a sandy beach-bar deposited in a shallow lake environment. The presence of wave bedding and parallel bedding (Fig. 11f) suggests that the facies was deposited by lake wave wash and agitation (Fraser and Hester, 1977; Zhu et al., 1994; Tucker, 2003; Jiang et al., 2011). The existence of mudstone pebbles and ripples (Fig. 11f) in the core indicates that the depth of the water was relatively shallow during the deposition of the sandy beach-bar, as described by Tucker (2003). We hypothesize that the linear distribution of the conglomerates and existence of pebbly sandstones (Fig. 11g) in the E_3e^L stage was caused by swashing erosions upon the bedrocks in the shallow lake. Therefore, we infer that this facies was deposited in an extremely shallow environment along the southern lower uplift (zone F).

4.2. Seismic facies analysis of beach and bar systems

The rock-physics relationships of the Palaeogene can be established in the study area using well-seismic calibration. Differences between the seismic facies (using typical seismic reflection characteristics) can be used to infer the underlying geology (Mitchum et al., 1977; Vail et al., 1977). Two typical seismic facies of beach and bar sand bodies are recognized in the study area.

4.2.1. Rock-physics relationships analysis

Lithology-velocity relationships can be established to predict the lithology in seismic (attribute) profiles effectively using seismic polarity or amplitude. Specifically, Palaeogene intervals in the study area mainly consist of mudstone, shaly sandstone, siltstone and

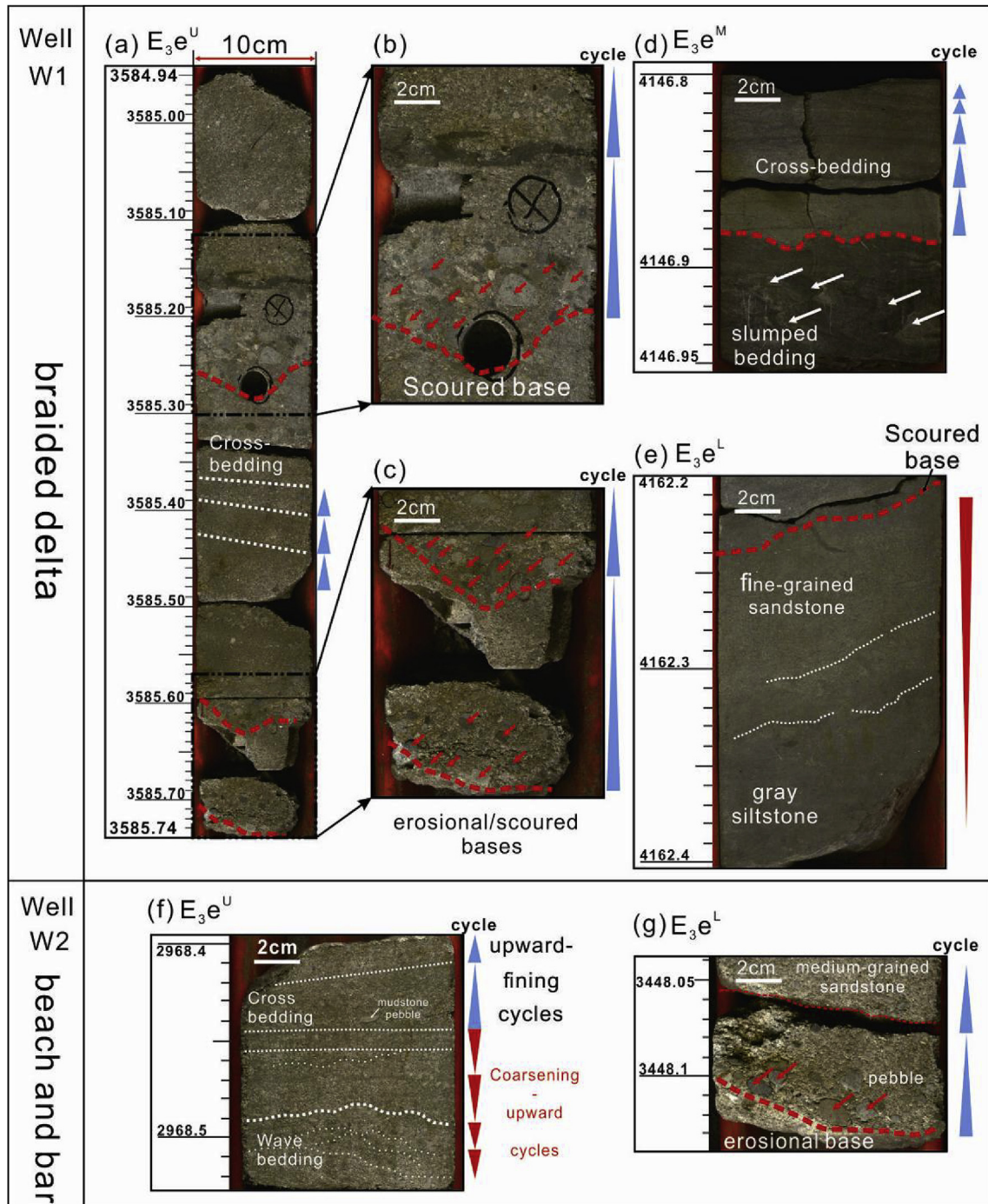


Fig. 11. Lithofacies of the Enping Formation. (a) Conglomeratic sandstones and coarse-grained to fine-grained sandstones with wedge-shaped cross-bedding and erosional bases (well-W1, 3584.94–3585.74 m, E_3e^U). (b) Conglomeratic sandstone with scoured base (well-W1, 3585.12–3585.30 m, E_3e^U). (c) Conglomeratic sandstone with erosional or scoured bases (well-W1, 3585.57–3585.74 m, E_3e^U). (d) Fine sandstone with trough-shaped cross bedding in the upper part and sandy mudstone with slumped bedding in the lower part (well-W1, 4146.8–4146.95 m, E_3e^M). (e) Fine-grained sandstones and siltstones in coarsening-upward interval (well-W1, 4162.2–4162.4 m, E_3e^L). (f) Fine-to medium-grained sandstones with mudstone pebbles and ripples in the upper part and fine-grained sandstones with micro-wavy bedding in the lower part (well-W2, 2968.4–2968.52 m, E_3e^U). (g) Massive positive rhythm conglomeratic sandstones (well-W2, 3448.04–3448.1 m, E_3e^L). The position of Fig. 11a, b, c, and d are shown in Fig. 3b, while the position of Fig. 11f and g are shown in Fig. 14b.

fine-grained sandstone interbedded with sandstone and shale. Fig. 12a shows a crossplot of the shale content and impedance in the study area, and different coloured points in the figure indicate different types of lithology: red points represent sandstone, black points represent mudstone, and yellow points represent a transitional type between mudstone and sandstone, such as shaly

sandstone. Different coloured points are distributed in different impedance-value zones. Generally, sandstone has a high impedance, and mudstone has a low impedance. The impedances of the different lithologies overlap by certain amounts, and an impedance of approximately $(1.0-1.1) \times 10^4$ m/s·g/cm³ divides sandstone and mudstone.

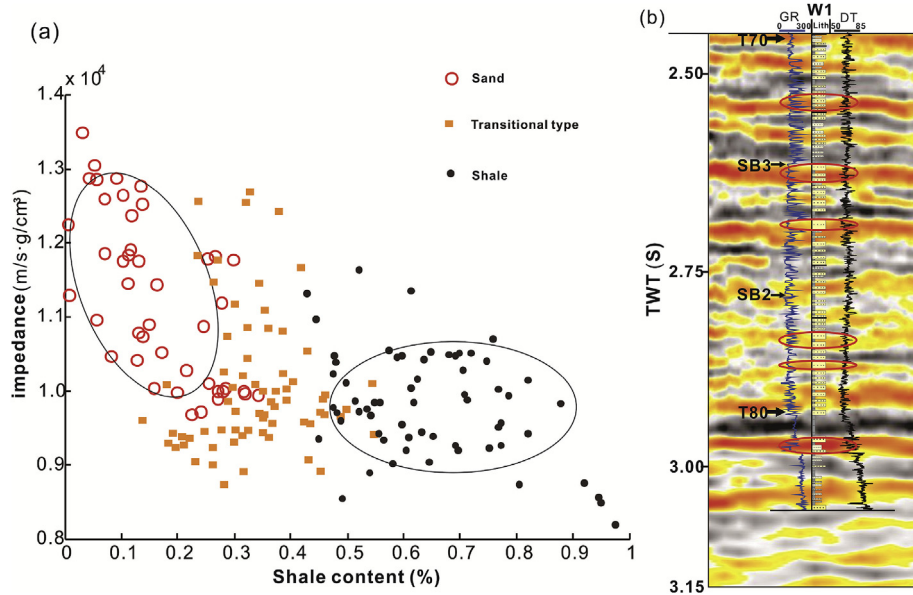


Fig. 12. Shale content-wave impedance relationship (a) and sandstone content correlated with average velocity of seismic events (b) in the Eocene Wenchang and Oligocene Enping Formations in W1.

Additionally, lesser or greater degrees of complexity in the lithology-decomposition analyses using seismic reflections are needed to define whether a single seismic event represents a single lithology or complex lithology (Zeng et al., 2012). In the study area, thin-bedded sandstone interbedded with mudstone is common. Therefore, no simple relationship exists between the sandstone bed and seismic event. Seismic events represent only average impedance changes between sandstone-prone (high sand-shale ratio, red peak) and mudstone-prone units (low sand-shale ratio, black trough). In Fig. 12b, the seismic peak events correlate with high average velocity intervals in the sonic log, which in turn correlate with a high sandstone content in the core section, even though the seismic trough events point in the opposite direction.

4.2.2. Typical seismic facies interpretation in the E₂W^U

Slope break belts, which usually constrain the development of specific facies zones, tend to form oil and gas accumulation zones in depositional system tracts. Slope break belts are currently one of the most important areas for in-depth reservoir exploration (Prather, 2003; Paton et al., 2008; Alfaro and Holz, 2014). In the past decade, a series of analyses (e.g. Lv et al., 2008; Chen et al., 2008; Zeng et al., 2015) were applied to beach-bar sand bodies (Fig. 13a) in the southern slope break of E₂W^U in the Enping Sag.

Based on phenomena related to gas measurement anomalies, high-pressure anomalies, the small size of the ground temperature gradient and AVO attribute anomalies of beach-bar sand bodies, Lv et al. (2008) inferred that sand bodies are favourable exploration areas with good oil-bearing properties. Schlumberger INC (2009) revealed that beach-bar sand bodies greater than 100 m could form the high-amplitude reflections seen Fig. 13b and c, depending on the AVO pre-stack inversion (Zeng et al., 2015).

On the basis of previous studies, seismic facies of beach and bar sand bodies are represented by sheet-like or mound-shaped reflections framed by high amplitude, low frequency and continuous reflections (Fig. 13 b–c). Based on a meticulous depiction of the 3-D beach and bar reflection characteristics, four beach-bar sand bodies with E-W-trends (I ~ IV) developed at the southern slope break belts (Fig. 13a), as revealed by the parallel seismic reflections in the seismic cross section aa' (Fig. 13b). Three beach-bar sand bodies (I, II

III) with lateral accretion reflections can be seen in the seismic cross section bb' (Fig. 13c). In particular, beach and bar sand bodies mainly formed by the short-axis delta (Zhu et al., 1994) are seen as wedge-shaped progradational seismic reflections in Fig. 13a and b.

4.2.3. Typical seismic facies interpretation in the E₃

During the depositional stage of the Enping Formation, the subsidence centre migrated from north to south (Wang et al., 2011). Typical seismic profiles along BB' (Fig. 1b) with wells W1, W2 and W3 were selected from the high resolution 3D seismic survey. The direction from W3 to W2 (SSE) is associated with faulted-trough sediment-transport pathway III, and it is nearly vertical to zone F. Furthermore, the direction from W2 to W1 (WNW) is associated with pathway I, and it is nearly parallel to zone F. The seismic reflection profiles are shown in Fig. 14.

1) E₃e^L

Sediments that are close to the depocenter of E₃e^L are characterized by sub-parallel (W3 block in Fig. 14a) and wedge-shaped progradational seismic reflections (W1 block in Fig. 14a). In addition, the medium-weak amplitude and medium-low continuous mound seismic reflections (No. I blue box in Fig. 14a) are between wells W1 and W2.

In the southern lower uplift (Zone F), the seismic facies are irregular to chaotic, with discontinuous lateral accretion reflections in the left area of W2, whereas seismic facies in the right area are parallel to roughly irregular and form semi-continuous reflections with the local development of clinoform sets (Fig. 14c). In this stage, the provenance of the beach and bar deposits is mainly bedrock of the southern Panyu lower uplift.

2) E₃e^M

The principal seismic facies around the W3 block comprises roughly parallel reflections with some locally formed poorly-defined channels (Fig. 14a). However, within the front-end of the section that corresponds to the mound-shaped reflections noted above, clinoform geometries (No. II blue box in Fig. 14a) are evident

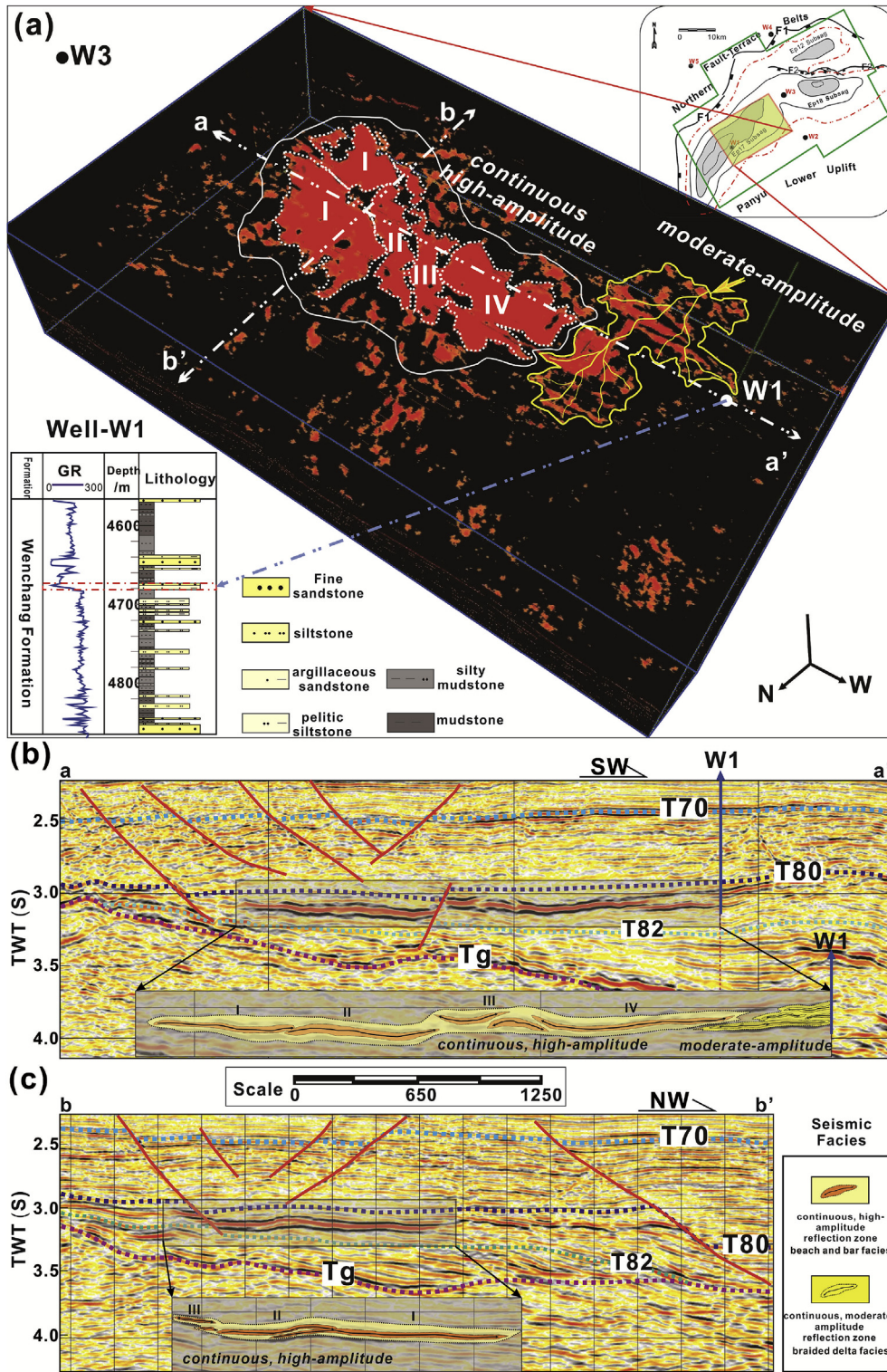


Fig. 13. Seismic cross section of the beach and bar sand bodies in the upper part of the Wenchang Formation (E_2W^U) in the southern slope of the Enping Sag. (a) 3-D distribution of beach and bar depositional systems. (b) Seismic cross sections aa', which runs east–southwest–west–northeast, and (c) bb', which runs east–northwest–west–southeast, which show the presence of subparallel (b), small-scale progradational seismic reflections (c) near the Panyu lower uplift on the southern slope of the Enping Sag. See Fig. 13a for the location of the seismic cross sections.

from the seismic data. In the W1 block, seismic reflections similar to those of E_3e^L are interpreted as delta-front deposits (Fig. 14a). Moreover, the mound-shaped seismic reflections (no. III blue box in Fig. 14a) migrated to zone F.

The gradient of the southern lower uplift zone (Zone F) is reduced to 1.0–1.6°. The seismic facies in the left of the W2 block comprises moderate continuity, moderate frequency, high amplitude and roughly lateral accretion reflections (Fig. 14c). Within the

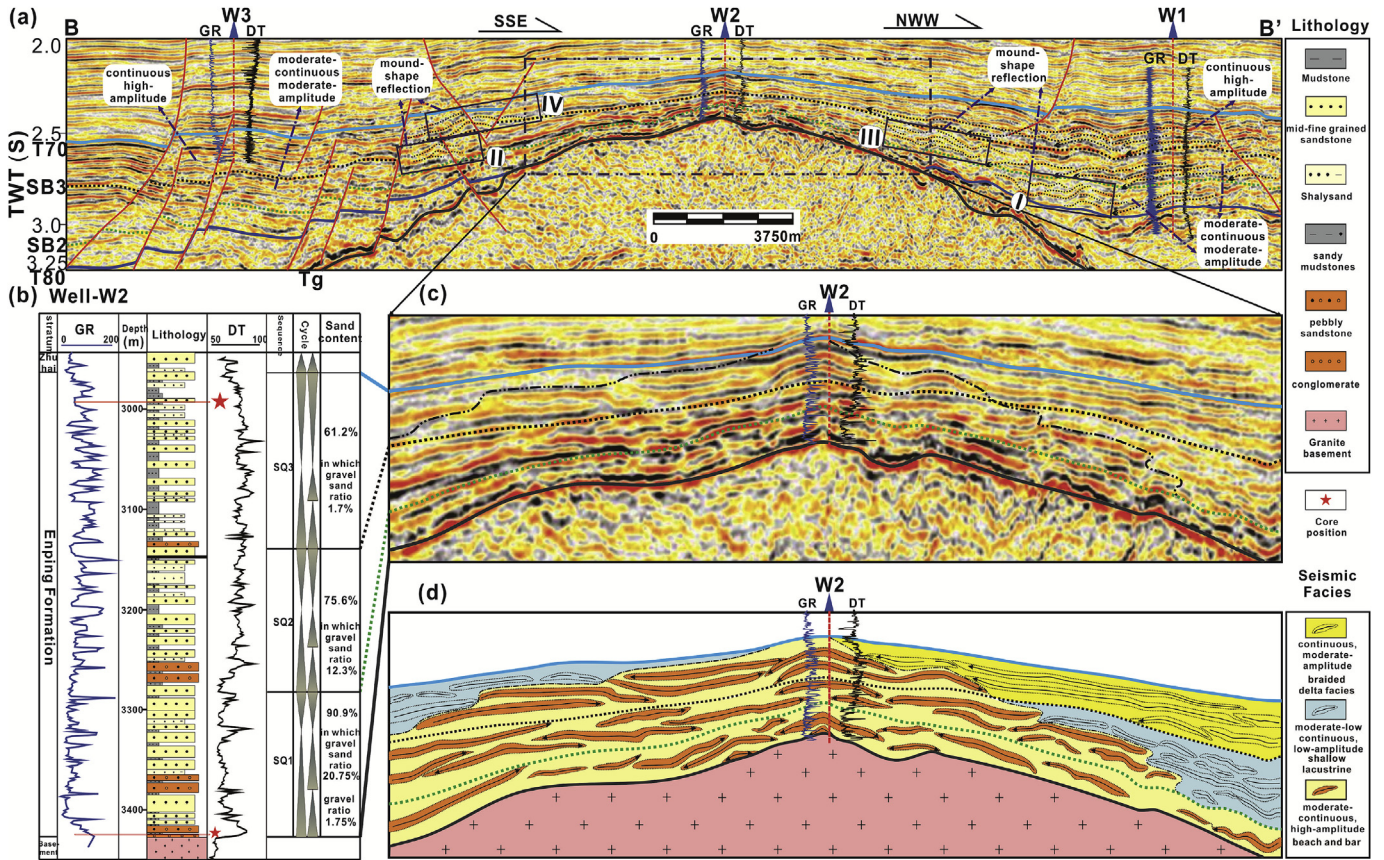


Fig. 14. Seismic facies characteristics of beach and bar bodies in the Enping Formation in the southern low uplift zone of the Enping Sag. (a) The seismic cross section BB' along the east-northwest–southeast–west-northwest directions, shows wedge-shaped, confluence seismic reflections. (b) The W2 profile with gamma-ray log, base-level cycles and lithology. (c) The uninterpreted and (d) interpreted lines of the typical seismic cross section shown in Fig. 14a, which show parallel, subparallel and progradational seismic reflections on the southern lower uplift zone. See Fig. 1b for the location of the seismic cross section (BB'). The red pentagrams represent the core positions used in Fig. 11.

right section, the seismic facies is the sub- or parallel reflection in the upper part of figure (black dotted boundary shown in Fig. 14c) and moderate-low amplitude, low continuous sub-parallel reflection in the lower part (blue section shown in Fig. 14d). In this stage, the bedrock supplies gradually weakened, so the range of beach and bar deposits narrowed relative to that for E_3e^L .

3) E_3e^U

The seismic facies of the W3 block is mainly characterized by a sub-parallel and concordant reflection framed by moderate amplitude and continuity (Fig. 14a). The mound-shaped seismic reflections (No. IV blue box in Fig. 14a) migrate and expand to zone F to the right of W3. In the W1 block, the seismic facies comprises the imbricate progradational seismic reflections and concordant reflection characteristics framed by moderate-high amplitude and continuity reflections (Fig. 14a). Furthermore, the moderate amplitude and continuous parallel seismic reflections have no obvious intersection between W1 and W2 (Fig. 14c).

In the southern lower uplift zone (between 0.5° and 1.0° generally), the seismic reflection boundary (black dotted) around the W2 block can be identified in Fig. 14c. Left of W2, the lower part mainly comprises lateral accretion reflections, whereas the discontinuous reflection thins upward on the southern lower uplift in the upper part (Fig. 14c). However, deposits mainly are characterized by a continuous and small-scale mound-shaped seismic facies in the right section (Fig. 14c). At that stage, as the source supplement of the South China fold belts continued to be enhanced,

sediment crossed over the southern lower uplift (zone F), whereas the range of the beach and bar deposits shrank and was dramatically reduced (Fig. 14d).

In the Eocene Wenchang and Oligocene Enping Formations, the beach and bar deposits were mainly supplied by southern and northern provenances on the southern lower uplift with low dips, subdued topography and shallow lacustrine water. The bedrock supplies on the southern Panyu lower uplift weakened from the bottom (E_2w^U) to top (E_3e^U), and the supplies of braided delta in the South China fold belts became enhanced. In addition, as the sand or conglomerate content of beach and bar deposits decreased continuously, they transformed from gravel-rich (E_3e^L) to sand-rich (E_3e^U), and thus the petrophysical properties of the beach and bar reservoir improved gradually.

4.3. Planar distribution of beach and bar systems

Well-control seismic multi-attribute analyses can be used to analyse the planar distribution of sedimentary facies. As a tool used to assist seismic interpretations, the purposes of multi-attribute analysis are to increase the efficiency of interpretation and the prediction accuracy of seismic attributes, to reduce the intuitive uncertainty and multiplicity and to lower exploration risk (Chopra et al., 2004; Kashihara and Tsuji, 2010; Raeesi et al., 2012; Zhu et al., 2014a, 2014b).

The workflow of a multi-attribute analysis begins with a sensitivity analysis of each extracted seismic single attribute to evaluate its contribution to the improvement of the correlations among the

seismic signal, lithofacies and logging facies. Then, a supervised clustering is performed to improve the correlation between the seismic information and core/log facies. The procedure includes a selection of training data from the core and wireline log-calibrated seismic data near the bore hole, followed by a neural network classification using a back propagation algorithm. As a result, multiple single attributes are combined to produce a seismic facies classification map (James et al., 2002; Coleou et al., 2003; Zhu et al., 2014a, 2014b).

In this study, three single attributes, the root mean square (RMS) amplitude attribute, instantaneous frequency (IF) instantaneous attribute and the bandwidth (BW) spectral attribute, were used individually to distinguish the depositional facies. These attributes, which were designated as a seismic facies classification index, were combined to form one new attribute by using a supervised neural network classification method (Raeesi et al., 2012) calibrated with the well data (Fig. 11 and Table 1). In the resulting seismic facies classification maps (Figs. 15a–18a), three types of facies were identified based on supervised learning for nonlinear relationships among the sandstone content and the seismic attributes near the borehole. The red facies refers to sand-rich sediments, the blue facies represents mud-rich sediments, and the yellow facies is a transitional facies containing a mixture of sandstone and mudstone.

4.3.1. Sediment patterns in the E_2W^U

Fig. 15a shows the planar distribution of the seismic multi-attributes in E_2W^U . The sand-rich and transitional sedimentary facies to the south of the Panyu lower uplift or zone E are typical narrow belts or sheet-shaped (slope break belt in the EP 17 subsag), which are distributed regularly in the areas between the north-east–southwest-trending slope systems and area perpendicular to those slopes. This indicates that sediments supplied from the Panyu lower uplift or zone E were transported for a relatively short distance and deposited through the incised valleys. In contrast, the gravel or sand-rich sedimentary facies (yellow or blue facies) near the northern fault-terrace belts generally show fan-like or lobate shapes distributed at the foot of the bounding faults (F1, F2). This suggests that the sediments derived from the South China fold belts were proximal with rapid accumulation. The shapes and distribution of the seismic multi-attribute anomalies clearly indicate that the sediments derived from the southern Panyu lower uplift or zone E and the northern South China fold belts are different in terms of their transport pathways, transport capacities and sedimentation ranges.

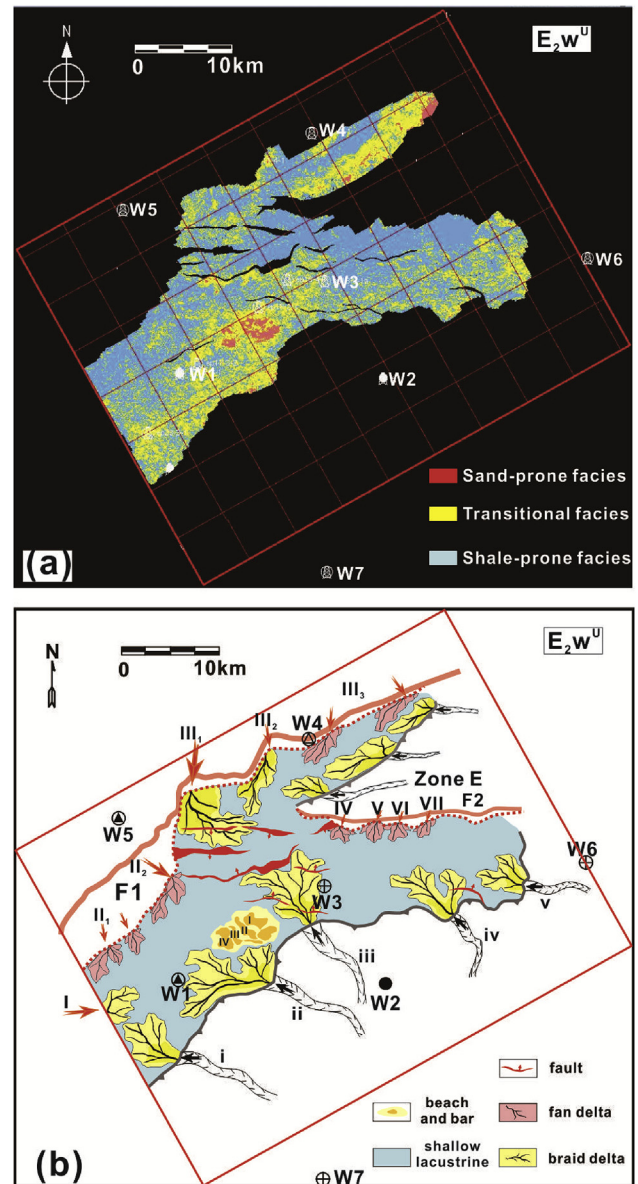


Fig. 15. Seismic facies classification map (a) and interpreted sedimentary facies map (b) of the upper member of the Wenchang Formation (E_2W^U), 3D area of Enping Sag.

Table 1
Relationship between drilling lithologies, lithofacies and seismic multi-attribute anomalies.

Formation	Member	Well	Assemblage of lithology	Sandstone percent	Depositional subfacies	Seismic multi-attribute
Enping	E_3e^U	W1	Thinly bedded (2–4 m), light-gray siltstone and gray mudstones with multiple coal beds	50.2%	Braided delta	Yellow facies
		W2	Thinly interbedded, fine-grained sandstones and siltstones in coarsening-upward intervals	61.2%	Beach-bar (sandy)	Red to yellow facies
		W3	Gray mudstones and sandy mudstones containing thin-bedded sandstones	30.2%	Shallow lacustrine	Blue facies
	E_3e^M	W1	Moderate-bedded (4–8 m), fine- to medium-grained sandstones in coarsening-upward intervals	60.1%	Braided Delta front	Yellow facies
		W2	Moderate-bedded, Conglomeratic sandstones, fine- to medium-grained sandstones, with thin mudstone	75.6%	Beach-bar (gravelly)	Red facies
	E_3e^L	W1	Thick-bedded, fine-grained to medium-grained sandstone, with thin siltstone, mudstone	61.2%	Braided Delta front	Yellow facies
W2		Thick-bedded (8–12 m), Conglomeratic sandstones and coarse-grained to fine-grained sandstones	90.9%	Beach-bar (gravelly)	Red facies	
Wenchang	E_2W^U	W1	Thinly bedded gray siltstone and argillaceous siltstone and massive dark mudstones with calcareous shells	26.8%	Shallow lacustrine	Blue facies

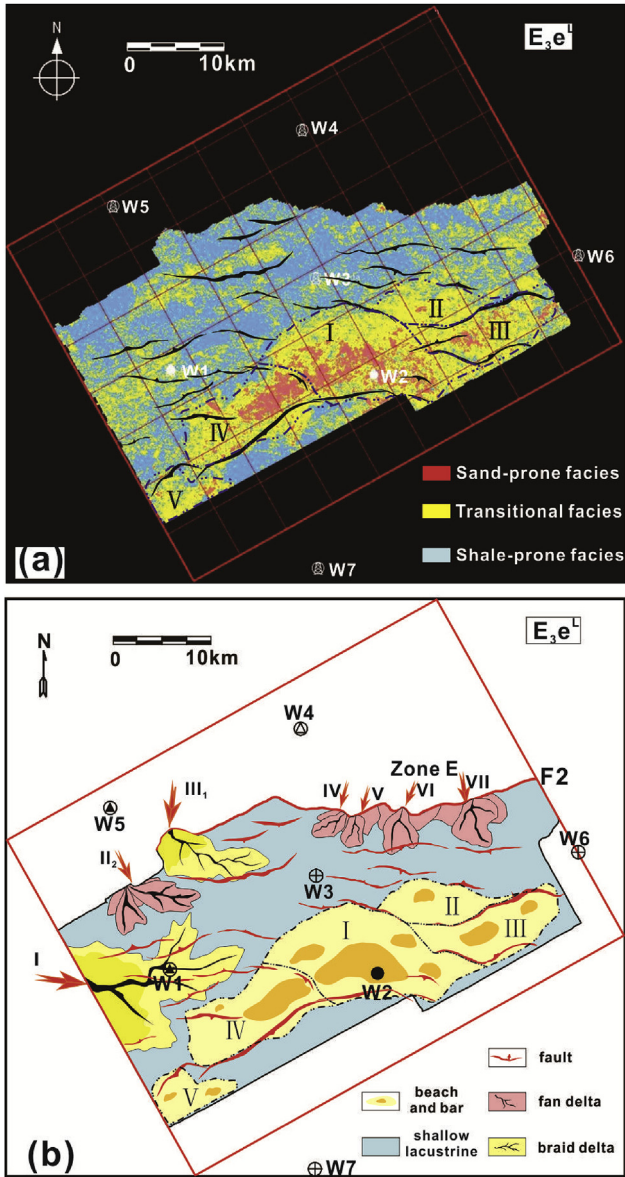


Fig. 16. Seismic facies classification map (a) and interpreted sedimentary facies map (b) showing the characteristics of the beach and bar systems in the lower member of the Enping Formation (E_3e^L), 3D area of the Enping Sag.

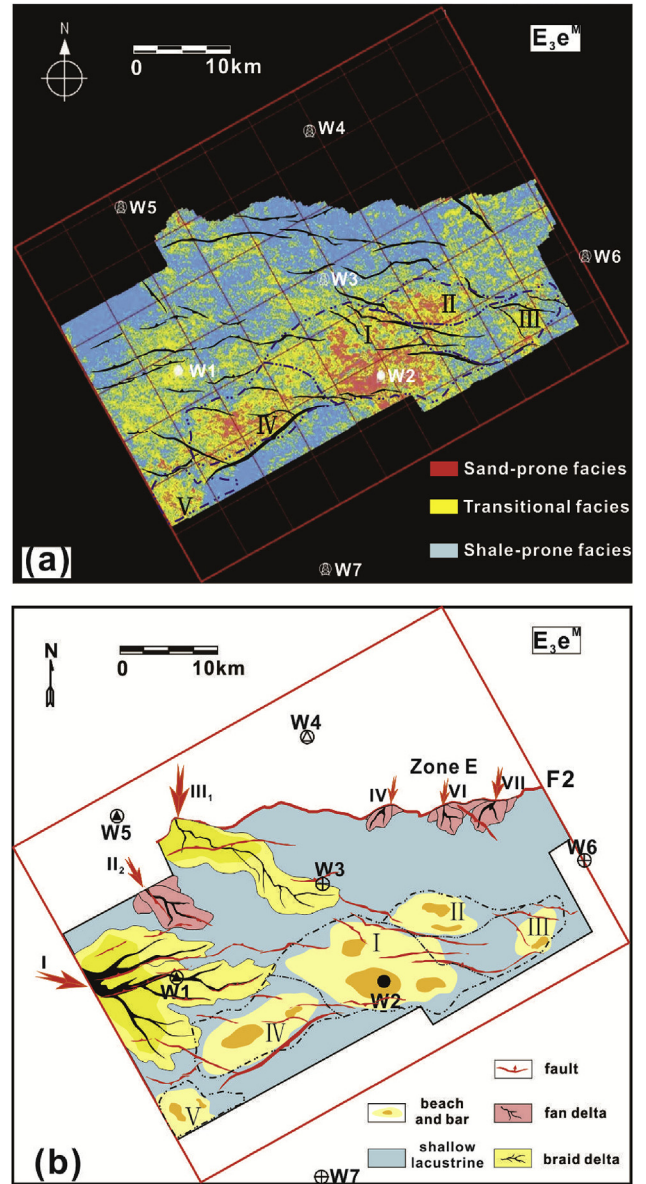


Fig. 17. Seismic facies classification map (a) and interpreted sedimentary facies map (b) showing the characteristics of the beach and bar systems in the middle member of the Enping Formation (E_3e^M), 3D area of the Enping Sag.

A final interpretation of the depositional facies was made using the vertical seismic facies analysis (Fig. 13b and c) and was calibrated using the well-based sedimentological analysis (Fig. 13a; Table 1) on the basis of the seismic multi-attribute anomalies (Fig. 15a).

Fig. 15b shows the planar distribution of the sedimentation facies interpreted from the multi-attributes and seismic facies. The deltaic deposits to the north of the Panyu lower uplift or zone E experienced relatively short distance (6–10 km) transportation through the several migrated incised valleys (e.g., i, ii, iii and iv) and were deposited as regular belts along the northeast–southwest trending. Additionally, the beach and bar deposits (approximately 42 km²), which were supplied by the short-axis braided deltas (with an area of 54–60 km²), are located in the southern slope-break belt, which is a potential favourable reservoir. However, there are nine fan-like and lobate-shaped fans distributed at the foot of the hanging wall of the bounding fault (five moderate-scale

fans adjacent to syn-fault F1 and other small-scale fans in syn-fault F2, distributed in the margin of the northern fault-terrace belts), which mainly were transported by faulted-trough pathways (II, III₃, IV, V, VI and VII), are characteristic of rapidly accumulated proximal fan deltas (Zeng et al., 2014, 2015) (with an area of 6–10 km²). In addition, three sheet-shaped fans distributed on the relatively slower topography or transfer belt in the north, which were transported by pathways I, III₁ and III₂, are characteristic of stable braided deltas (Wang et al., 2011; Zeng et al., 2014, 2015) (with an area of 25–40 km²). Additionally, the mostly blue or muddy facies in the central part of the study area are interpreted as shallow lacustrine facies.

4.3.2. Sediment patterns in the E_3e

The southern low uplift area can be divided into five blocks, namely blocks I, II, III, IV and V, based on the palaeotopography, seismic facies, seismic multi-attribute anomalies and differences in

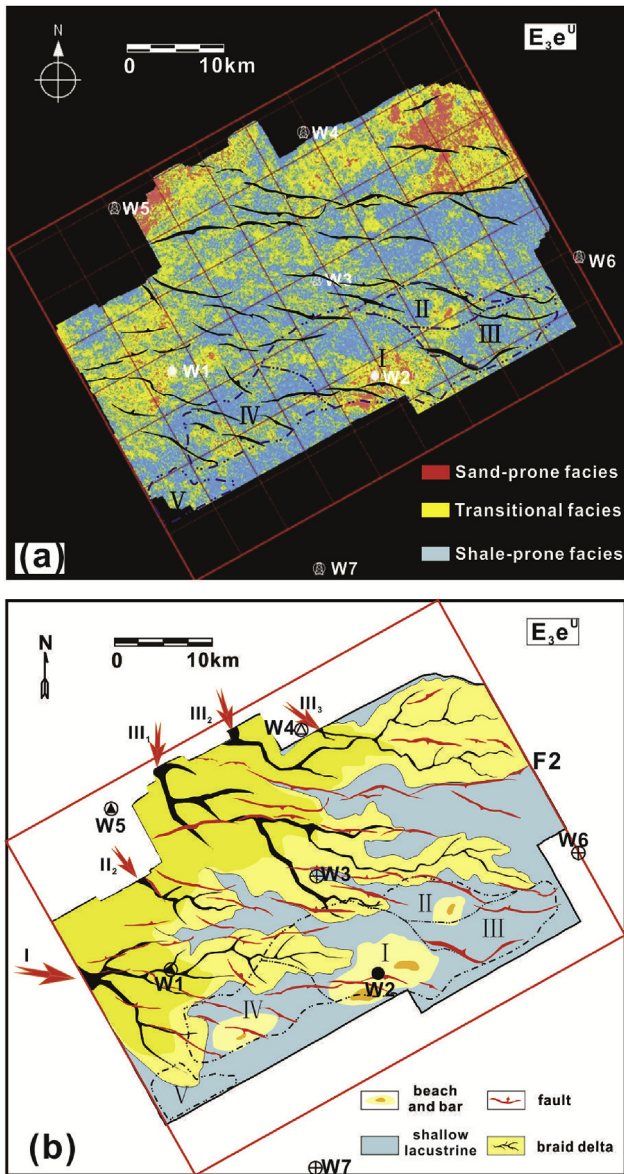


Fig. 18. Seismic facies classification map (a) and interpreted sedimentary facies map (b) showing the characteristics of the beach and bar systems in the upper member of the Enping Formation (E_3e^U), 3D area of the Enping Sag.

the fracture systems. The distribution patterns of the beach and bar systems can be analysed in the Palaeogene third-order sequence unit of the Enping sag, with different supplied sedimentary systems.

1) E_3e^L

During the deposition of E_3e^L , the study area experienced a maximum tectonic subsidence and constantly rising lake level in the Enping Formation. The accommodation space at the root of the hanging wall of the boundary faults (F1 and F2) increased, which resulted in the delivery of the sediments from the South China fold belts by the faulted-trough sediment-transport pathways (I ~ VII), and the southern lower uplift subsided to the subaqueous high. The sediments then entered the depositional area and rapidly accumulated at the root of the boundary fault in the north and around the southern subaqueous high.

On the seismic multi-attribute map of E_3e^L (Fig. 16a), the yellow and blue facies dominate the fan-shaped distributions with different scales at the root of the hanging wall of the boundary faults (F1, F2), whereas the red and yellow facies are manifested by sheet-shaped distributions with large-scale at the southern subaqueous high. The depositional facies map was produced based on the lithofacies definition of each coloured facies (Fig. 16b). The sedimentological characteristics of wells W1 and W2 show that the sand bodies of E_3e^L are mainly composed of several fining-upward cycles, as interpreted from the wireline-log patterns and lithological associations (see Figs. 3b, 11 and 14; Table 1). The well-seismic tie shows wedge-shaped progradational patterns in W1 and mound-shaped stacking patterns in W2 (Fig. 14). The well-based sedimentary facies, seismic facies and seismic sedimentology-derived facies architecture jointly indicate that fan- or sheet-shaped and lobate seismic multi-attribute anomalies (e.g., red and yellow facies) are proximal fan-deltas or braided deltas with rapid accumulations in the north and gravelly beach-bar in zone F. Most of the blue areas in the central part of the study area are interpreted as shore facies or shallow lacustrine facies (Fig. 16b).

The northern fans, which are controlled by the palaeotopography and the main source from pathway I to VII, are typical fan-shaped proximal fan deltas with wedge-shaped chaotic seismic facies and rapid accumulation (approximately 32–45 km²), which are similar to deposits in the Baiyun sag (Mi et al., 2008). Two small-scale lobate braided deltas had experienced relatively long-distance (12–16 km) transportation and were deposited as regular belts along the second-order fault trending (northwest-southeast-trending) in the northwestern margin (pathway I, with an area of 125 km²) and transition belt (pathway III, with an area of 78 km²) of the Enping sag (Fig. 16b). The delta front sediments migrated and deposited in blocks I, IV and V (zone F) through fault-trough pathway I under the control of the lake-wave, lake-flow and landform. Furthermore, the southern fans, which were controlled by a low gradient (1.5–2.8°) subaqueous high, are gravel-rich bar systems located along the uplift with a long and narrow banding structure (from gravelly bar, sandy beach to shallow lacustrine facies) in a planar distribution (Fig. 16b). These beach and bar deposits, which are in the southern subaqueous high with an area of 342 km², correspond to basement rock. They are generally composed of conglomeratic sandstones and fine- to medium-grained sandstones with poor reservoir quality.

2) E_3e^M

During the deposition of E_3e^M , the tectonic activity weakened gradually, and the base level continued to rise leading to a complete drowning of the Panyu lower uplift to form the depositional area (Fig. 6). The base-level rise caused its surface to move landward, to enlarge the area of the positive accommodation space and to increase the sediment storage capacity.

On the seismic multi-attribute map of E_3e^M (Fig. 17a), the red and yellow facies in the depositional area (mainly in the southern subaqueous high) are characterized by a long-term inherited development. The fan-shaped seismic multi-attribute anomalies still can be observed at the root of the hanging wall of the boundary fault and southern subaqueous high, similar to those in E_3e^L . The fan-shaped or lobate seismic multi-attribute anomalies (yellow and blue facies) developed at the root of the hanging wall of the boundary fault (F1, F2) are interpreted as a slumped delta front (subaqueous fan) caused by fault activation through pathways II, IV, VI and VII or braided delta through pathways I (shown in W1) and III. The sheet-shaped multi-attribute anomalies (red and yellow facies) that develop on the southern lower Uplift (seen in W2) are believed to have been formed in a gravel-rich beach-bar

depositional environment (Fig. 14 and Table 1). The blue or argillaceous facies in the central part of the study area is interpreted as a shore facies or shallow lacustrine facies (Fig. 17b).

Two braided deltas with an area of 176 km² and 110 km², which have experienced relatively long-distance (20 km) transport along pathways I and III, increase in the north. The delta front sediments correspond to the migration and expansion of pathway III to W3. Meanwhile, the braided delta depositional area further enlarged through fault-trough pathway I (entering into zone F), and the transport capacity of the source had also expanded to blocks I, IV and V. In addition, the southern beach and bar sedimentary system with moderate continuity and a sheet-like northeast-southwest trend in the plane, was reduced to 296 km² (Fig. 17b). The gravel-rich bar and sand-rich beach systems are mainly confined to blocks I, II and IV, which indicates that the gravel and sand contents in the beach-bar decreased, the basement rock supplies weakened and northern braided deltas supplies increased relative to those of the E₃e^L stage.

3) E₃e^U

During the deposition of E₃e^U, the base level began to fall continuously and tectonic activity weakened gradually, which led to the Ep 12 subsag and formation of sediment source areas in zone E. The available accommodation zone shifted basinward, so that sediments could be transported basinward when lake-level fell (Coe et al., 2003). More sediments were bypassed through the northern uplifts (zone E) and extended outward of the central part. As a result, band- or fan-shaped red and yellow seismic facies multi-attributes are widely developed from the north to south (Fig. 18a). This sequence is mainly dominated by a deltaic deposition (Figs. 11 and 14; Table 1).

On the seismic multi-attribute map of E₃e^U (Fig. 18a), the red and yellow facies that are located at the root of the hanging wall of the boundary fault (F1) predominantly display band- or fan-shaped distributions. More sediments in E₃e^U accumulated toward the basin centre after long-distance transport, compared to the seismic multi-attribute distributions of E₃e^L and E₃e^M. Thus, the large-scale progradational seismic reflections (Fig. 14a), seismic sedimentology analysis (Figs. 11 and 14b) and the band-shaped seismic multi-attribute anomalies are interpreted as braided deltaic deposition through pathways I, II and III (northwest-southeast-trending). The mud-prone area shown by the blue anomalies in the southeastern part of the study area is believed to be a shallow lacustrine facies (Fig. 18b).

The delta–plain deposits with red and yellow facies developed at the root of the hanging wall of the boundary fault (F1) along the planar distribution of three faulted troughs, whereas the fan-delta front deposits with yellow facies develop in the basin centre or EP 12 subsag. Braided deltas experienced long-distance (26–35 km) transportation and covered the original beach and bar system with an area of 364–482 km² towards the south. In addition, the beach and bar deposits in blocks I, II and IV decrease significantly (with an area of 76 km²) in comparison to E₃e^L and E₃e^M and disappear in blocks III and V (Fig. 18b). In this stage, the beach and bar systems, which are generally composed of fine- to medium-grained sandstones with good reservoir quality, primarily come from the northern multi-point sourced braided delta front (by pathways I and II). The oil saturation is higher near the top of the coarsening-upward sandstones.

4.4. Dispersal pattern of the beach and bar systems

According to their locations and sedimentary features, beach and bar systems in rift lacustrine basins (Enping Sag) may be

divided into two types: beach-bar systems supplied by the short-axis delta (E₂w) and beach-bar systems on subaqueous high (E₃e). Specifically, different genetic types and planar distribution laws of beach and bar systems are associated with the sedimentary systems in the southern subaqueous high. In the study area, sedimentary system modelling can be divided into bedrock-beach bar system and braided delta–beach bar system based on the relationship between provenance and the beach and bar deposits.

Variations exist in the Palaeogene beach and bar system models within the different blocks of southern lower uplift in the Enping Sag. In the E₂w^U stage, the sand-rich beach-bar deposits supplied by the short-axis delta that developed widely over the slope break belt have good reservoir qualities (Fig. 15). Subsequently, a bedrock-beach bar system developed on the subaqueous high with a relatively poor reservoir quality and a large-scale continuous gravel-rich beach bar during the E₃e^L stage (Fig. 16). During the E₃e^M stage, the bedrock-beach bar system transformed to mixed sources, including a gravelly bedrock-beach bar and sandy braided delta–beach bar system (Fig. 17). As the ratio of the gravel or sand, continuity and sedimentary range of the beach and bar systems decreased, the reservoir quality improved. Lastly, the sandy braided delta–beach bar system corresponds to the reduced sandstone content and depositional range of the beach and bar systems during the E₃e^U stage (Fig. 18).

5. Conclusion

The integration of sequence stratigraphy and seismic sedimentology allowed an analysis of the provenance system and mapping sediment-dispersal patterns of the beach and bar deposits in the Palaeogene third-order sequence framework of the Enping Sag, Pearl River Mouth Basin. The following conclusions can be drawn.

- 1) Palaeogeomorphological features reveal that three faulted-trough sediment-transport pathways (I, II and III) trending northwest-southeast developed in the north of Enping Sag and that four or five migrated incised-valleys (i, ii, iii₁, iii₂ and iv) developed in the south.
- 2) The provenances were a composite source system in Palaeogene and mainly consisted of Palaeozoic metamorphic rocks and Mesozoic igneous rocks, with supplementary Proterozoic metamorphic rocks. On the upper member of the Wenchang Formation (E₂w^U), a single type of Mesozoic igneous grains was derived from the basement of the southern Panyu lower uplift. In the Enping Formation (E₃e), mixed types of Palaeozoic metamorphic, Mesozoic igneous and a few Proterozoic metamorphic grains are mainly ascribed to the basement of the South China fold belts and the Panyu lower uplift. In the Zhuhai Formation (E₃z), predominant metamorphic grains are associated with the basement of the South China fold belts. The Palaeozoic and Proterozoic metamorphic grain contents gradually increase in the Enping Formation from the base (E₃e^L) to the top (E₃e^U), and the Mesozoic igneous grain content obviously decreases.
- 3) Two types of Palaeogene beach and bar systems appear in the Enping Sag: the beach-bar system supplied by the short-axis delta, as mainly developed in E₂w^U, and the beach-bar developed on the subaqueous high in E₃e. Specifically, the sedimentary system model transformed from a bedrock-beach bar system (E₂w^L) to a braided delta–beach bar system in the Enping Formation (E₂w^U). These beach-bars are regularly distributed at the gentle slope or subaqueous high of a lacustrine basin through basin evolution. The oil-gas exploration indicates that beach-bar deposits are able to accumulate oil-gas on the subaqueous high and become important targets for hydrocarbon exploration.

Acknowledgements

This study was supported by the National Natural Science Foundation of China (No. 41572084), the Henry Fok Education Foundation (132020), and Major National Science and Technology Programs in the “Twelfth Five-Year” Plan period (No. 2011ZX05023-001-015, 2011ZX05001-002-01). We are grateful to the Salvatore Critelli, anonymous reviewers and Massimo Zecchin, the Associate Editor of Marine and Petroleum Geology, for their constructive comments and suggestions, which have greatly improved the manuscript. The Shenzhen Branch of the China National Offshore Oil Corporation is thanked for providing data used in this study and the permission to publish the results.

References

- Alfaro, E., Holz, M., 2014. Seismic geomorphologic analysis of deepwater gravity-driven deposits on a slope system of the southern Colombian Caribbean margin. *Mar. Pet. Geol.* 57, 294–311.
- Allen, P.A., 2005. Striking a chord. *Nature* 434, 961.
- Allen, P.A., 2008a. From landscapes into geological history. *Nature* 451, 274–276.
- Allen, P.A., 2008b. Time scales of tectonic landscapes and their sediment routing systems. In: Gallagher, K., Jones, S.J., Wainwright, J. (Eds.), *Landscape Evolution: Denudation, Climate and Tectonics over Different Time and Space Scales*, Special Publications, 296. Geological Society, London, pp. 7–28.
- Allen, P.A., Hovius, N., 1998. Sediment supply from landslide-dominated catchments: implications for basin-margin fans. *Basin Res.* 10, 19–35.
- Arribas, J., Critelli, S., Le Pera, E., Tortosa, A., 2000. Composition of modern stream sand derived from a mixture of sedimentary and metamorphic rocks (Henares River, central Spain). *Sediment. Geol.* 133, 27–48.
- Bhatia, M.R., 1983. Plate tectonics and geochemical composition of sandstones. *J. Geol.* 91, 611–627.
- Blatt, H., Tooten, M.W., 1981. Detrital quartz as an indicator of distance from shore in marine mudrocks. *J. Sediment. Petrol.* 51 (4), 1259–1266.
- Bonjour, J.L., Dabard, M.P., 1991. Ti/Nb ratios of clastic terrigenous sediments used as an indicator of provenance. *Chem. Geol.* 91 (3), 257–267.
- Brandon, M.T., Garver, J.I., 1994. Provenance studies of Columbia–England by fission tracks analysis. *Chem. Geol.* 89, 37–52.
- Briaïsi, A., Patriat, P., Tapponnier, P., 1993. Updated interpretation of magnetic anomalies and seafloor spreading in the South China Sea: implications for the tertiary tectonics of Southeast Asia. *J. Geophys. Res.* 98 (B4), 6299–6328.
- Chen, C.M., 2000. Petroleum geology and conditions for hydrocarbon accumulation in the eastern Pearl River Mouth Basin. *China Offshore Oil Gas. (Geol.)* 14, 73–83 (in Chinese with English abstract).
- Chen, G.J., Lv, C.F., Li, Y.L., He, S.B., Wang, T.Q., Liu, D.W., Du, G.C., 2008. Analysis of the oil- and gas-bearing turbidite within wenchang formation in eeping depression, Pearl River mouth Basin, China. *Acta Sedimentol. Sin.* 26 (5), 881–885 (in Chinese with English abstract).
- Chen, S.Z., Pei, C.M., 1993. Geology and geochemistry of source rocks of the eastern Pearl River mouth Basin, South China sea. *J. SE Asian Earth Sci.* 8, 393–406.
- China geological Atlas of editorial board, 2002. *Geological Atlas of Chinese*. Geology Publishing House, Beijing, pp. 253–260 (in Chinese).
- Chopra, S., Alexeev, V., Pruden, D., 2004. Non-linearity in multi-attribute analysis-tackling. *First Break* 22, 43–48.
- Coe, A.L., Bosence, D.W.J., Church, K.D., Flint, S.S., Howell, J.A., Wilson, R.C.L., 2003. *The Sedimentary Record of Sea-level Change*. Cambridge University Press, London, pp. 58–73.
- Coleou, T., Poupon, M., Azbel, K., 2003. Unsupervised seismic facies classification: a review and comparison of techniques and implementation. *Lead. Edge* 22 (10), 942–953.
- Contreras, J., Scholz, C.H., King, G.C.P., 1997. A general model of rift basin evolution: constraints of first order stratigraphic observations. *J. Geophys. Res.* 102, 7673–7690.
- Cope, T., Luo, P., Zhang, X.Y., Zhang, X.J., Song, J.M., Zhou, G., Shultz, M.R., 2010. Structural controls on facies distribution in a small half-graben basin: Luanping basin, northeast China. *Basin Res.* 22, 33–44.
- Critelli, S., Rumelhart, P.E., Ingersoll, R.V., 1995. Petrofacies and provenance of the Puente formation (Middle to upper miocene), Los Angeles Basin, southern California: Implications for rapid uplift and accumulation rates. *J. Sediment. Res.* A65, 656–667.
- Critelli, S., Le Pera, E., Ingersoll, R.V., 1997. The effects of source lithology, transport, deposition and sampling scale on the composition of southern California sand. *Sedimentology* 44, 653–671.
- Critelli, S., Mongelli, G., Perri, F., Martin-Algarra, A., Martin-Martin, M., Perrone, V., Dominici, R., Sonnino, M., Zaghoul, M.N., 2008. Sedimentary evolution of the Middle Triassic–lower Jurassic continental redbeds from Western-Central Mediterranean Alpine Chains based on geochemical, mineralogical and petrographical tools. *J. Geol.* 116, 375–386.
- Cullen, A., Reemst, P., Henstra, G., Gozzard, S., Ray, A., 2010. Rifting of the South China Sea: new perspectives. *Petrol. Geosci.* 16, 273–282.
- Dai, Y.D., Pang, X., 1999. Petroleum geological characteristics of zhu ii depression, Pearl River mouth Basin. *China Offshore Oil Gas. (Geol.)* 13, 169–173 (in Chinese with English abstract).
- Davis, W.M., 1989. The rivers and valleys of Pennsylvania. *Natl. Geogr. Mag.* 1, 183–253.
- Deng, H.W., Guo, J.Y., Wang, R.J., Xie, X.J., 2008. Tectonic sequence stratigraphic analysis in continental faulted basins. *Earth Sci. Front.* 15 (2), 1–7 (in Chinese with English abstract).
- Densmore, A.L., Allen, P.A., Simpson, G., 2007. Development and response of a coupled catchment fan system under changing tectonic and climatic forcing. *J. Geophys. Res. Earth Surf.* 112, 16.
- Dickinson, W.R., 1985. Interpreting provenance relations from detrital modes of sandstones. In: Zuffa, G. (Ed.), *Provenance of Arenites*, Nato-asi (Series 1), 48. D. Reidel, Dordrecht, pp. 333–361.
- Dumont, T., Schwartz, S., Guillot, S., Simon-Labric, T., Tricart, P., Jourdan, S., 2012. Structural and sedimentary records of the Oligocene revolution in the Western Alpine arc. *J. Geodyn.* 56–57, 18–38.
- Folk, R.L., 1974. *Petrology of Sedimentary Rocks*. Hemphill, Austin, Texas, p. 182.
- Franke, D., 2013. Rifting, lithosphere breakup and volcanism: comparison of magma-poor and volcanic rifted margins. *Mar. Petrol. Geol.* 43, 63–87.
- Franke, D., Savva, D., Pubellier, M., Steuer, S., Mouly, B., Auxietre, J., Meresse, F., Chamot-Rooke, N., 2014. The final rifting evolution in the South China Sea. *Mar. Petrol. Geol.* 58, 704–720.
- Fraser, G.S., Hester, N.C., 1977. Sediments and sedimentary structures of a beach-ridge complex, southwestern shore of Lake Michigan. *J. Sediment. Petrol.* 47, 1187–1200.
- Frelinger, S.N., Ledvina, M.D., Richard Kyle, J., Zhao, D.G., 2015. Scanning electron microscopy cathodoluminescence of quartz: Principles, techniques and applications in ore geology. *Ore Geol. Rev.* 65, 840–952.
- Fu, N., Ding, F., He, S.B., Zhang, G.C., 2007. Source rocks evaluation and reservoir characteristics analysis in Enping sag, Pearl River Mouth basin. *China Offshore Oil Gas* 19 (5), 295–299, 305 (in Chinese with English abstract).
- Fu, N., He, S.B., Zhang, G.C., 2009. Hydrocarbon accumulation period and age in eeping depression, Pearl River Estuary Basin. *Bull. Mineral., Petrol. Geochem.* 28 (1), 42–47 (in Chinese with English abstract).
- Gawthorpe, R.L., Leeder, M.R., 2000. Tecto-sedimentary evolution of active extensional basins. *Basin Res.* 12, 195–218.
- Gong, Z., Li, S., Xie, T., Zhang, Q., Xu, S., Xia, K., Yang, J., Sun, Y., Liu, L., 1997. Continental Margin Basin Analysis and Hydrocarbon Accumulation of the Northern South China Sea. Science Press, Beijing, p. 510 (in Chinese).
- Guangdong Province Bureau of Geology and Mineral Resources, 1988. *Regional Geology of Guangdong Province*. Geological Publishing House, Beijing, pp. 1–941 (in Chinese).
- Gupta, S., Cowie, P.A., Dawers, N.H., Underhill, J.R., 1998. A mechanism to explain rift-basin subsidence and stratigraphic patterns through fault-array evolution. *Geology* 26 (7), 595–598.
- Haddad, S.C., Worden, R.H., Prior, D.J., Smalley, P.C., 2006. Quartz cement in the Fontainebleau sandstone, Paris basin, France: crystallography and implications for mechanisms of cement growth. *J. Sediment. Res.* 76, 244–256.
- Henza, A.A., Withjack, M.O., Schlische, R.W., 2009. Normal-fault development during two phases of non-coaxial extension: an experimental study. *J. Struct. Geol.* 32 (11), 1656–1667.
- Hsiao, L.Y., Graham, S., Tilander, A.N., 2010. Stratigraphy and sedimentation in a rift basin modified by synchronous strike-slip deformation: southern Xialiao basin, Bohai, offshore China. *Basin Res.* 22 (1), 61–78.
- Huang, B.J., Xiao, X.M., Zhang, M.Q., 2003. Geochemistry, grouping and origins of crude oils in the Western Pearl River Mouth Basin, offshore South China Sea. *Org. Geochem.* 34, 993–1008.
- Huang, X., 1989. Study of sources of Paleozoic granitoids and the basement of South China by means of Nd-Sr isotope. *Acta Petrol. Sin.* 1, 28–36 (in Chinese with English abstract).
- Hunt, A.M.W., 2013. Development of quartz cathodoluminescence for the geological grouping of archaeological ceramics: firing effects and data analysis. *J. Archaeol. Sci.* 40, 2902–2912.
- Jackson, S.E., Pearson, N.J., Griffin, W.L., Belousova, E.A., 2004. The application of laser ablation-inductively coupled plasma-mass spectrometry to in-situ U–Pb zircon geochronology. *Chem. Geol.* 220, 47–69.
- James, H., Peloso, A., Wang, J., 2002. Volume interpretation of multi-attribute 3D surveys. *First Break* 20 (3), 176–180.
- Jiang, D.X., Yang, H.Q., 2000. Original environment of Eocene petroleum source rocks in the Pearl River Mouth Basin. *Acta Sedimentol. Sin.* 18, 469–474 (in Chinese with English abstract).
- Jiang, Z.X., Liu, H., Zhang, S.W., Su, X., Jiang, Z.L., 2011. Sedimentary characteristics of large-scale lacustrine beach-bars and their formation in the Eocene Boxing Sag of Bohai Bay Basin, East China. *Sedimentology* 58, 1087–1112.
- Kashihara, K., Tsuji, T., 2010. Improvement in facies discrimination using multiple seismic attributes for permeability modelling of the Athabasca Oil Sands, Canada. *Explor. Geophys.* 41 (1), 80–87.
- Leeder, M.R., 2011. Tectonic sedimentology: sediment systems deciphering global to local tectonics. *Sedimentology* 58 (1), 2–56.
- Li, P.L., Rao, C.T., 1994. Tectonic characteristics and evolution history of the Pearl River Mouth Basin. *Tectonophysics* 235, 13–25.
- Li, P.L., Liang, H.X., Dai, Y.D., 1998. Exploration perspective of basement hydrocarbon accumulations in the Pearl River Mouth Basin. *China Offshore Oil Gas Geol.* 12 (6), 361–369 (in Chinese with English abstract).

- Li, X.H., 2000. Cretaceous magmatism and lithospheric extension in Southeast China. *J. Asian Earth Sci.* 18, 293–305.
- Li, Y.C., Tao, W.X., Sun, Y.M., He, S.B., He, Q., 2009. Classification and distribution of oil in Huizhou depression of Pearl River mouth Basin. *Acta Pet. Sin.* 30 (6), 830–834 (in Chinese with English abstract).
- Li, Z.X., Li, X.H., 2007. Formation of the 1300 km-wide intracontinental orogen and postorogenic magmatic province in Mesozoic South China: a flat-slab subduction model. *Geology* 35, 179–182.
- Lin, C.S., Zheng, H.R., Ren, J.Y., Liu, J.Y., Qiu, Y.G., 2004. The control of syndepositional faulting on the Eocene sedimentary basin fills of the Dongying and Zhanhua sags, Bohai Bay rift basin. *Sci. China (Series D)* 47 (9), 769–782 (in Chinese with English abstract).
- Liu, L.H., Chen, S.H., Yu, S.M., Xiong, J.Y., Jiang, J., Xu, X.M., Liu, X.L., Hu, K., 2011. Analyzing conditions of hydrocarbon accumulation and a commercial breakthrough in Enping sag, Pearl River Mouth basin. *China Offshore Oil Gas* 23 (2), 76–80 (in Chinese with English abstract).
- Liu, Q.H., 2013. Sequence Stratigraphic Architecture and Quantitative Simulation under the Low-angle Normal Fault in the Rifted Basin: Example from Wenchang Formation, Paleogene, Enping Sag. China University of Geosciences, Wuhan, pp. 30–46 (in Chinese).
- Liu, Q.H., Zhu, H.T., Shu, Y., Zhu, X.M., Yang, X.H., Fu, X., 2015. Provenance systems and their control on the beach-bar of Paleogene Enping formation, Enping sag, Pearl River mouth Basin. *Acta Pet. Sin.* 36 (3), 286–299 (in Chinese with English abstract).
- Liu, Q.H., Zhu, H.T., Yang, X.H., Shu, Y., Huang, Z., 2013. Quantitative recognition of seismic sequence stratigraphic units in wenchang formation, Paleogene, Enping sag, Pearl River mouth Basin. *J. Central South Univ. Sci. Technol.* 44 (3), 1076–1082 (in Chinese with English abstract).
- Liu, Y.S., Hu, Z.C., Gao, S., Günther, D., Xu, J., Gao, C.G., Chen, H.H., 2008. In situ analysis of major and trace elements of anhydrous minerals by LA-ICP-MS without applying an internal standard. *Chem. Geol.* 257 (1–2), 34–43.
- Lu, B.L., Wang, P.J., Zhang, G.C., Zhang, B., Sun, X.M., Li, W.Z., Lang, Y.Q., 2011. Basement structures of an epicontinental basin in the northern South China Sea and their significance in petroleum prospect. *Acta Pet. Sin.* 32 (4), 580–587 (in Chinese with English abstract).
- Lv, C.F., Chen, G.J., Wang, T.Q., Li, Y.L., He, S.B., Liu, D.W., 2008. Characteristics of lithology anomalous body in tertiary Wenchang formation of Enping Sag. *Acta Pet. Sin.* 29 (3), 368–371, 377 (in Chinese with English abstract).
- Ludwig, K.R., 2003. User's manual for Isoplot 3.0: a Geochronological toolkit for Microsoft excel Berkeley geochronology center. *Spec. Publ.* 4, 1–71.
- Martin, R., 1966. Paleogeomorphology and its application to exploration for oil and gas (with examples from western Canada). *AAPG Bull.* 10, 2277–2311.
- Masini, E., Manatschal, G., Mohn, G., Ghienne, J.F., Lafont, F., 2011. The tectono-sedimentary evolution of a supra-detachment rift basin at a deep-water magma-poor rifted margin: the example of the Samedan Basin preserved in the Err nappe in SE Switzerland. *Basin Res.* 23, 652–677.
- McLennan, S.M., Hemming, S., McDaniel, D.K., Hanson, G.N., 1993. Geochemical approaches to sedimentation, provenance, and tectonics. In: Johnson, M.J., Basu, A. (Eds.), *Processes Controlling the Composition of Clastic Sediments*. Geological Society of America Special Paper 284, pp. 21–40.
- Mi, L.J., Zhang, G.C., Shen, H.L., Liu, Z., Guo, R., Zhong, K., Tian, J.X., 2008. Eocene-lower oligocene sedimentation characteristics of Baiyun Sag in the deep water area of Pearl River Mouth Basin. *Acta Pet. Sin.* 29 (1), 29–34 (in Chinese with English abstract).
- Miller, E.L., Gehrels, G.E., Pease, V., Sokolov, S., 2010. Stratigraphy and U-Pb detrital zircon geochronology of Wrangel Island, Russia: implications for arctic paleogeography. *AAPG Bull.* 94 (5), 665–692.
- Mitchum Jr., R.M., Vail, P.R., Sangree, J.B., 1977. Seismic stratigraphy and global changes of sea level, Part 6: stratigraphic interpretation of seismic reflection patterns in depositional sequences. In: Payton, C.E. (Ed.), *Seismic Stratigraphy*. AAPG Memoir, 26, pp. 117–134.
- Morley, C.K., Back, S., 2008. Estimating hinterland exhumation from late orogenic basin volume, NW Borneo. *Geol. Soc. Lond.* 165 (1), 353–366.
- Morley, C.K., Nelson, R.A., Patton, T.L., Munn, S.G., 1990. Transfer zones in the East African rift system and their relevance to hydrocarbon exploration in rifts. *AAPG Bull.* 74 (8), 1234–1253.
- Morton, A.C., Todd, S.P., Haughton, D.W., 1991. Developments in sedimentary provenance studies. London, geological Society, London. *Spec. Publ.* 57, 370.
- Nemchin, A.A., Cawood, P.A., 2005. Discordance of the U–Pb system in detrital zircons: Implication for provenance studies of sedimentary rocks. *Sediment. Geol.* 182, 143–162.
- Olsen, P.E., 1997. Stratigraphic record of the early mesozoic breakup of Pangea in the Laurasia–Gondwana rift system. *Annu. Rev. Earth Planet. Sci.* 25, 337–401.
- Omer, M.F., Friis, H., 2014. Cathodoluminescence investigations on quartz cement in the sandstones of Khabour formation from Iraqi Kurdistan region, Northern Iraq. *J. Afr. Earth Sci.* 91, 44–54.
- Pang, X., Chen, C.M., Peng, D.J., Zhou, D., Shao, L., He, M., Liu, B.J., 2008. Basic geology of Baiyun deep-water area in the northern South China Sea. *China Offshore Oil Gas* 20, 216–222 (in Chinese with English abstract).
- Paton, D.A., van der Spuy, D., di Primio, R., Horsfield, B., 2008. Tectonically induced adjustment of passive-margin accommodation space; influence on the hydrocarbon potential of the Orange Basin. *South Africa. AAPG Bull.* 92, 589–609.
- Peacock, D.C.P., Knipe, R.J., Sanderson, D.J., 2000. Glossary of normal faults. *J. Struct. Geol.* 22 (3), 291–305.
- Perri, F., Critelli, S., Mongelli, G., Cullers, R.L., 2011. Sedimentary evolution of the Mesozoic continental redbeds using geochemical and mineralogical tools: the case of upper triassic to lowermost jurassic Monte di Gioiosa mudstones (Sicily, southern Italy). *Int. J. Earth Sci.* 100, 1569–1587.
- Perri, F., Critelli, S., Martin-Algarra, A., Martin-Martin, M., Perrone, V., Mongelli, G., Zattin, M., 2013. Triassic redbeds in the Malaguide complex (Betic Cordillera – Spain): petrography, geochemistry and geodynamic implications. *Earth Sci. Rev.* 117, 1–28.
- Posamentier, H.W., 2004. Seismic geomorphology: imaging elements of depositional systems from shelf to deep basin using 3D seismic data: implications for exploration and development. In: Davies, R.J., Cartwright, J.A., Stewart, S.A., Lappin, M., Underhill, J.R. (Eds.), *3D Seismic Technology: Applications to the Exploration of Sedimentary Basins*, Memoirs, 29. Geological Society, London, pp. 11–24.
- Posamentier, H.W., Davies, R.J., Cartwright, J.A., Wood, L., 2007. Seismic geomorphology an overview. In: Special Publication, 277. Geological Society, London, pp. 1–14.
- Prather, B.E., 2003. Controls on reservoir distribution, architecture and stratigraphic trapping in slope settings. *Mar. Pet. Geol.* 20, 529–545.
- Prizomwala, S.P., Bhatt Nilesh, Basavaiah, N., 2014. Provenance discrimination and Source-to-Sink studies from a dryland fluvial regime: an example from Kachchh, western India. *Int. J. Sediment Res.* 29, 99–109.
- Raeesi, M., Moradzadeh, A., Ardejani, F.D., Rahimi, M., 2012. Classification and identification of hydrocarbon reservoir lithofacies and their heterogeneity using seismic attributes, logs data and artificial neural networks. *J. Petroleum Sci. Eng.* 82–83, 151–165.
- Richards, M., Bowman, M., Reading, H., 1998. Submarine-fan systems i: characterization and stratigraphic prediction. *Mar. Petroleum Geol.* 15 (7), 689–717.
- Rosendahl, B.R., 1987. Architecture of continental rifts with special reference to East Africa. *Annu. Rev. Earth Planet. Sci.* 15, 445–503.
- Roser, B.P., Korsch, R.J., 1988. Provenance signatures of sandstone–mudstone suites determined using discriminant function analysis of major element data. *Chem. Geol.* 67 (1–2), 119–139.
- Ru, K., Pigott, J.D., 1986. Episodic rifting and subsidence in the South China Sea. *Bull. Am. Ass. Petrol. Geol.* 70, 1136–1155.
- Schlische, R.W., 1991. Half–graben basin filling models: new constraints on continental extensional basin development. *Basin Res.* 3 (3), 123–141.
- Schlische, R.W., Olsen, P.E., 1990. Quantitative filling model for continental extensional basins with applications to early mesozoic rifts of eastern North America. *J. Geol.* 98, 135–155.
- Schlische, R.W., Withjack, M.O., 2009. Origin of fault domains and fault–domain boundaries (transfer zones and accommodation zones) in extensional provinces—result of random nucleation and self–organized fault growth. *J. Struct. Geol.* 31 (9), 910–925.
- Sømme, T.O., Helland-Hansen, W., Martinsen, O.J., Thurmond, J.B., 2009. Relationships between morphological and sedimentological parameters in source-to-sink systems: a basis for predicting semi-quantitative characteristics in subsurface systems. *Basin Res.* 21, 361–387.
- Sømme, T.O., Jackson, C.A.-L., Vaksdal, M., 2013. Source-to-sink analysis of ancient sedimentary systems using a subsurface case study from the Møre-Trøndelag area of southern Norway: Part 1 – depositional setting and fan evolution. *Basin Res.* 25, 489–511.
- Sømme, T.O., Jackson, C.A.-L., 2013. Source-to-sink analysis of ancient sedimentary systems using a subsurface case study from the Møre-Trøndelag area of southern Norway: part 2 – sediment dispersal and forcing mechanisms. *Basin Res.* 25, 512–531.
- Stevenson, R.K., Whittaker, S., Mountjoy, E.W., 2000. Geochemical and Nd isotopic evidence for sedimentary– source changes in the Devonian mioecoline of the southern Canadian Cordillera. *Geol. Soc. Am. Bull.* 112 (4), 531–539.
- Su, D.Q., White, N., McKenzie, D., 1989. Extension and subsidence of the Pearl River mouth Basin, northern South China sea. *Basin Res.* 2, 205–222.
- Sun, Q.L., Wu, S.G., Cartwright, J., Wang, S.H., Lu, Y.T., Chen, D.X., Dong, D.D., 2014. Neogene igneous intrusions in the northern South China Sea: evidence from high-resolution three dimensional seismic data. *Mar. Petrol. Geol.* 54, 83–95.
- Sun, X.M., Zhang, X.Q., Zhang, G.C., Lu, B.L., Yue, J.P., Zhang, B., 2014. Texture and tectonic attribute of cenozoic basin basement in the northern South China Sea: Science China. *Earth Sci.* 57, 1199–1211 (in Chinese with English abstract).
- Sun, Z., Zhong, Z., Keep, M., Zhou, D., Cai, D., Li, X., Wu, S., Jiang, J., 2009. 3D analogue modeling of the South China Sea: a discussion on breakup pattern. *J. Asian Earth Sci.* 34, 544–556.
- Taylor, B., Hayes, D.E., 1983. Origin and history of the South China sea Basin. In: Hayes, D.E. (Ed.), *The Tectonic and Geologic Evolution of Southeast Asian Seas and Islands*. AGU, Washington, DC, pp. 23–56.
- Tucker, M.E., 2003. *Sedimentary Rocks in the Field*. John Wiley & Sons Ltd, West Sussex, UK, pp. 67–70.
- Vail, P.R., Mitchum Jr., R.M., Todd, R.G., Widmier, J.M., Thompson, S., Sangree, J.B., Bubb, J.N., Hatlelid, W.G., 1977. Seismic stratigraphy and global changes of sea level. In: Payton, C.E. (Ed.), *Seismic Stratigraphy*. AAPG Memoir, 26, pp. 49–212.
- Wang, J.H., Liu, L.H., Chen, S.H., Shang, Y.L., 2011. Tectonic–sedimentary responses to the second episode of the Zhu-Qiong movement in the Enping depression, Pearl River Mouth Basin and its regional tectonic significance. *Acta Pet. Sin.* 32 (4), 588–595 (in Chinese with English abstract).
- Wang, Z.J., Chen, H.D., Zhang, J.Q., 2000. The research and prospect in provenance analysis. *Sediment. Geol. Tethyan Geol.* 20 (4), 104–110 (in Chinese with English abstract).
- Wu, J., Ye, J.R., Shi, H.S., Chen, S.H., Liang, B., 2013. Overpressure forming and its

- effect on petroleum accumulation in central faulted structural belt of enping depression, China. *J. Central South Univ. Sci. Technol.* 44 (7), 2801–2811 (in Chinese with English abstract).
- Xu, X.B., Zhang, Y.Q., Jia, D., Shu, L.S., Wang, R.R., 2009. Early mesozoic geotectonic processes in South China. *Geol. China* 36 (3), 573–593 (in Chinese with English abstract).
- Xu, Y.J., Du, Y.S., Yang, J.H., 2007. Prospects of sediment provenance analysis. *Geol. Sci. Technol. Inf.* 26 (3), 26–32 (in Chinese with English abstract).
- Xue, L., 2013. Element Geochemistry Evaluation of Paleogene Source Rocks in Enping Depression. China University of Geosciences, Wuhan, pp. 34–35 (in Chinese).
- Yan, Q.S., Shi, X.F., Castillo, P.R., 2014. The late mesozoic–cenozoic tectonic evolution of the South China Sea: a petrologic perspective. *J. Asian Earth Sci.* 85, 178–201.
- Zeng, H.L., Hentz, T.F., 2004. High-frequency sequence stratigraphy from seismic sedimentology: applied to Miocene, Vermilion Block 50, Tiger Shoal area, offshore Louisiana. *AAPG Bull.* 88 (2), 153–174.
- Zeng, H.L., Zhu, X.M., Zhu, R.K., Zhang, Q.S., 2012. Guidelines for seismic sedimentologic study in non-marine postrift basins. *Petroleum Explor. Dev.* 39 (3), 295–304.
- Zeng, Z.W., Yang, X.H., Shu, Y., Chen, S.H., Liu, Q.H., Wu, J., Fu, X., 2014. Development characteristics and tectonic-sedimentary response of glutenite bodies of Wenchang formation in Northern steep slope, Enping Sag. *Geol. Sci. Technol. Inf.* 33 (6), 60–68 (in Chinese with English abstract).
- Zeng, Z.W., Yang, X.H., Shu, Y., Chen, S.H., Wu, J., Wang, W., Xia, C.C., 2015. Structure palaeogeomorphology characteristics and sand bodies distribution regularities of Paleogene Wenchang formation in enping sag: under the conditions of lack of drilling data to predict and evaluate the reservoir sand bodies. *Geoscience* 29 (4), 804–815 (in Chinese with English abstract).
- Zhang, B., Wang, P.J., Zhang, G.C., Sun, X.M., Lu, B.L., Ni, W.Y., 2013. Cenozoic volcanic rocks in the Pearl River Mouth and Southeast Hainan Basins of South China Sea and their implications for petroleum geology. *Petroleum Explor. Dev.* 40 (6), 704–713.
- Zhang, S.C., Liang, D.G., Gong, Z.S., Wu, K.Q., Li, M.W., Song, F.Q., Song, Z.G., Zhang, D.J., Wang, P.R., 2003. Geochemistry of petroleum systems in the eastern Pearl River Mouth Basin: evidence for mixed oils. *Org. Geochem* 34, 971–991.
- Zhang, X.H., 2008. Tectonic Geology in China Seas. China Ocean Press, Beijing, pp. 335–338 (in Chinese).
- Zhang, Y.Q., Xu, X.B., Jia, D., Shu, L.S., 2009. Deformation record of the change from Indosinian collision-related tectonic system to Yanshanian subduction-related tectonic system in South China during the Early Mesozoic. *Earth Sci. Front.* 16 (1), 234–247 (in Chinese with English abstract).
- Zhao, H.G., Liu, C.Y., 2003. Approaches and prospects of provenance analysis. *Acta Sedimentol. Sin.* 21 (3), 409–415 (in Chinese with English abstract).
- Zhu, H.T., Yang, X.H., Zhou, X.H., Liu, K.Y., 2014a. Three-dimensional facies architecture analysis using sequence stratigraphy and seismic sedimentology: example from the Paleogene Dongying Formation in the BZ3-1 block of the Bozhong Sag, Bohai Bay Basin, China. *Mar. Petroleum Geol.* 51, 20–33.
- Zhu, H., Yang, X.H., Liu, K.Y., Zhou, X.H., 2014b. Seismic-based sediment provenance analysis in continental lacustrine rift basins: an example from the Bohai Bay Basin, China. *AAPG Bull.* 98 (10), 1995–2018.
- Zhu, W.L., Li, M.B., Wu, P.K., 1999. Petroleum system of zhu iii sub-basin, Pearl River mouth Basin, south China sea. *AAPG Bull.* 83, 990–1003.
- Zhu, W.L., Mi, L.J., 2010. Atlas of Oil and Gas Basins. Petroleum Industry Press, China Sea, p. 102 (in Chinese).
- Zhu, X.M., Xin, Q.L., Zhang, J.R., 1994. Seimentary characteristics and models of the beach-bar reservoirs in faulted down lacustrine basins. *Acta Sedimentol. Sin.* 12 (2), 20–28 (in Chinese with English abstract).
- Zhou, D., Sun, Z., Chen, H.Z., Xu, H.H., Wang, W.Y., Pang, X., Cai, D.S., Hu, D.K., 2008. Mesozoic paleogeography and tectonic evolution of South China Sea and adjacent areas in the context of Tethyan and Paleo-Pacific interconnections. *Isl. Arc* 17, 186–207.
- Zhuo, H.T., Wang, Y.M., Shi, H.S., Zhu, M., He, M., Chen, W.T., Li, H., 2014. Seismic geomorphology, architecture and genesis of miocene shelf sand ridges in the Pearl River Mouth Basin, northern South China Sea. *Mar. Petrol. Geol.* 54, 106–122.
- Zhuo, X.Z., Wang, Q., Chen, G.J., Lv, C.F., 2007. Vertical Porosity variation of clastic reservoir rock in Enping sag, Zhujiangkou Basin. *Nat. Gas. Geosci.* 18 (5), 643–647, 666 (in Chinese with English abstract).
- Zong, K.Q., Liu, Y.S., Gao, C.G., Hu, Z.C., Gao, S., Gong, H.J., 2010. In situ U-Pb dating and trace element analysis of zircons in thin sections of eclogite: refining constraints on the ultra-high pressure metamorphism of the Sulu terrane, China. *Chem. Geol.* 269, 237–251.